Transportation Geotechnics 48 (2024) 101299

Contents lists available at ScienceDirect

Transportation Geotechnics

journal homepage: www.elsevier.com/locate/trgeo

Original Article

Machine learning-based modeling of interface creep behavior of grouted soil anchors with varying soil moistures

Genbao Zhang [a,b], Changjie Xu [b], Di Wang [c], Yufei Wang [d], Junbo Sun [c,*], Shimin Zhu [e], Amr M. Morsy [f], Zhonghe Liu [g], Xiangyu Wang [b]

[a] *College of Civil Engineering, Hunan City University, Yiyang, Hunan 413000, China*
[b] *School of Civil Engineering and Architecture, East China Jiaotong University, Nanchang 330013, Jiangxi, China*
[c] *Institute for Smart City of Chongqing University in Liyang, Chongqing University, Jiangsu 213300, China*
[d] *School of Design and Built Environment, Curtin University, Perth, WA 6102, Australia*
[e] *School of Civil Engineering, Ludong University, Yantai 264025, China*
[f] *Department of Civil Engineering & Construction Engineering Management, College of Engineering, California State University Long Beach, CA 90840, United States*
[g] *Liyang Market Comprehensive Inspection and Testing Center, Jiangsu, 213300, China*

ARTICLE INFO

Keywords:
Grouted soil anchor
Pullout test
Machine learning
BAS-BPNN
Interface creep behavior

ABSTRACT

The interface creep behavior of the grouted soil anchor subject to varying soil moisture was investigated using the combined incorporation of experimental and data-driven modeling methods to establish an efficient and robust forecasting framework. This study carried out the rapid and creep pullout tests of element anchor specimens at various saturations and then utilized machine learning methods to predict the development of interface creep displacement. The stepwise loading strategy and nonlinear superposition method were combined to generate the interface shear creep curves of the element anchor specimens. A total of 936 data groups of the interface shear displacement were collected with changing soil moisture contents, interface shear time, and interface shearing stress. Next, this study explored the Back Propagation Neural Network (BPNN) and four other machine learning algorithms in predicting the interface creep behavior of the grouted soil anchor under various moisture conditions. As for the hyperparameters, the beetle antennae search (BAS) approach was employed to optimize the BPNN and random forest (RF) models. Finally, the boxplot and Taylor diagrams proved the BAS-BPNN demonstrated a better performance than BAS-RF in predicting the interface creep behavior. The consequent correlation coefficients ranged from 0.9613 to 0.9805 for BPNN, indicating the accuracy and reliability of the interface creep prediction. A partial dependence plot (PDP) was also introduced to visualize the established machine learning model. The threshold of moisture content near 28.7 % is found to switch the interface shear stress-displacement response from strain-stabilizing to strain-softening behavior and to result in the main moisture-increase-induced interface strength degradation. The soil moisture fluctuation leads to the development of interface shear displacement mainly observed in the early phase of 20 h after the onset of moisture change. The uncovered coupled impact of soil moisture condition and interface shear stress state can provide insights into the evaluation of the time-dependent in-service performance of grouted soil anchors embedded in clayey soils.

Introduction

Clay widely distributed in China, presents an inevitable challenge for geotechnical engineers who are seeking for a solution to implement the balance between the construction of underground structures and the ecosystem health [1,2]. The ground constituted of clayey soil is observed to be characterized with insufficient bearing capacity and excessive deformation due to the strain-softening behavior of clayey soil [3].

Ground anchors have emerged as an effective solution to stabilize the clayey soil by transferring the unstable zone-induced loads posing on the underground structures to the stable zone in the extended ground [4–6]. For example, grouted soil anchors are often employed to prevent the uplifts of basement embedded in the ground with increasing groundwater tables, due to the merits of low cost, rapid curing, ease of

---

* Corresponding author.

E-mail addresses: genbao@hncu.edu.cn (G. Zhang), xucj@zju.edu.cn (C. Xu), 202116131002@cqu.edu.cn (D. Wang), tunneltc@gmail.com (J. Sun), smzhu@ldu.edu.cn (S. Zhu), Amr.Morsy@csulb.edu (A.M. Morsy), Xiangyu.Wang@curtin.edu.au (X. Wang).

https://doi.org/10.1016/j.trgeo.2024.101299
Received 8 October 2023; Received in revised form 9 June 2024; Accepted 12 June 2024

installation, and application versatility [7]. However, it is reported that the failure of the interface between the anchor and the ground poses a serious threat to the long-term service of anchored structures [8–10]. To ensure the in-service performance of anchored structures, the accurate prediction and optimal design of interface behavior of grouted soil anchors under varying environmental conditions are crucial to prevent debonding failure over the anchor-soil interface [11,12].

Many researchers have formulated empirical bond-slip models to promptly characterize the interface bond behavior by testing the pullout response of ground anchors [13]. However, compared with the modeling of the interface behavior of ground anchors under short-term (rapid) loading, the modeling of the interface creep behavior of the ground anchor accounting for the time effect was few reported [14–17], especially with considerations of varying ground conditions.

The long-term in-service performance of the grouted soil anchor is dependent on the creep behavior of materials constituting the anchor, including the reinforcement, the grout, the soil, and the interfaces between each other [14]. Compared with that of the reinforcement and the grout, the soil creep [18,19] and the soil-anchor interface creep [12] contribute at large to the long-term behavior of the grouted soil anchor due to the varying environmental conditions of the soil and the soil-structure interaction with time-lag effect [20]. The ground soils surrounding the anchor can be saturated differently due to rainfall infiltration and underground seepage, which results in the change of pullout response for the ground anchor [11,21]. In particular, it is observed that a slight increase in the moisture content of the soil can trigger creep failure at the soil-anchor interface under high shear stress [12]. Therefore, it is critical to consider the coupled effect of loading level and moisture condition in predicting the interface creep behavior of the grouted soil anchor.

Due to the capability of controlling and modeling the ground conditions and anchor installation precisely for the ground anchor in practice, the pullout test on the element anchor specimens is used widely to characterize the interface behavior under both the rapid loading [22,23] and the long-term loading [13–15,17] conditions. However, the combinations of specific ground conditions (e.g., soil compaction, soil moisture) and anchor installation (e.g., the anchor size, the grouting material) can lead to the requirement of remarkable element anchor specimens in anchor interface characterization using pullout test, which implies unacceptable time-consuming and budget costs.

Machine learning (ML) algorithms provide strong support to laboratory tests in geotechnical engineering by establishing combined physical-data-driven modeling based on limited testing data obtained in laboratory tests to make predictions and decisions without explicit programming. The long short-term memory (LSTM), deep neural networks (DNN), K-nearest neighbor (KNN), Gaussian process regression (GPR), support vector regression (SVR), and decision tree (DT) were used to forecast the uniaxial compressive strength of different types of rock based on the dataset from basic physical and mechanical parameters tested in the laboratory [24]. The effectiveness and efficiency of the back propagation neural network (BPNN) combined with particle swarm optimisation (PSO), and the random forest (RF) with hyperparameters tuned by the firefly algorithm (FA), were compared elaborately in predicting the interface bond behavior of glass fiber reinforced polymer embedded in cemented soils [25,26]. Three single machine learning algorithms (K-nearest neighbor, neural network, and decision tree) and two ensemble learning algorithms (random forest and extreme gradient boosting) were used to establish a machine learning-based framework for predicting the permanent strain accumulation of unbound aggregates based on the dataset from the tested material properties and stress states of aggregate specimens [27]. The artificial neural networks was employed to develop the fatigue model characterizing the coupled impact of the traffic loading paramters, the physical paraters of the soil on the permanent deformation of the railway track beds, which demonstrated high prediction reliability and accuracy [28]. The AutoGluon automatic machine learning framework was applied to establish the intelligent evaluation model for the geostress levels based on a multi-index fusion database of the range-based indecies indentified from collected documents [29]. Seven machine learning models were used in comparison to develop a new pedotransfer function for estimating the soil water characteristic curve of unsaturated soils based on the dataset from physical parameters (pressure head, soil textural information, state parameters, and particle density) tested in the laboratory [30]. Among the abovementioned ML tools, artificial neural networks (ANN) demonstrate comparative competence in terms of their applicability to solving geotechnical problems due to its strong generalization ability, fault tolerance ability, memory association, parallel architecture, and nonlinear mapping [31].

Table 1
The physical and mechanical parameters of the clayey soil sample.

Parameters (unit)	Value
Natural moisture content, w_0 (%)	31.5
Wet density, ρ (g/cm^3)	1.91
Specific gravity, G_s	2.7
Plastic index, PI (%)	25.6
Liquid limit, LL (%)	45.2
Average void ratio, e_0	1.1
Uniformity coefficient, C_u	4.9
Coefficient of curvature, C_c	0.6
Cohesion, c (kPa)	55.3
Internal friction angle, ϕ (°)	12.0

Therefore, the combined physical-data-driven modeling framework was adopted consecutively to characterize the interface creep behavior of grouted soil anchors installed in clayey soils with varying moisture conditions. The pullout creep test used a device specially designed to facilitate moisture conditioning and a comparatively short embedment length [22,23]. The dependent variable in this study was the interface shearing displacement, while the independent variables were the moisture content of clayey soil, the shearing time, and the interface shearing stress. The study will explore machine learning (ML) methods, including back propagation neural network (BPNN), random forest (RF), and baseline models, to predict the interface creep behavior of grouted soil anchors. Furthermore, the beetle antennae search (BAS) approach and 10-fold cross-validation will be used to adjust the algorithm's structure. The best ML method will be determined based on the results from the boxplot and Taylor diagrams. This investigation elucidates the interconnectedness between the moisture condition of the ground soil and the external stress on the soil-anchor interface, thereby providing insight into their combined effects on the interface creep behavior of the grouted soil anchor embedded in clayey soils. The investigation aims to provide a rapid prediction of the time-dependent in-service performance of grouted soil anchors in practice.

Experimental programs

Materials

The clayey soil used in this study was obtained from the Xiangjiang River in Changsha, China. The soil samples were purified, mixed evenly, and sealed in a laboratory environment for 48 h to ensure uniform moisture distribution. Subsequently, the physical and mechanical parameters of the soil were tested necessarily in the laboratory, as shown in Table 1. The clayey soil samples were poorly graded because the coefficient of uniformity and the coefficient of curvature were less than 5 and 1, respectively (Fig. 1). The grout material used in this study was cement mortar with a mixing ratio of water, cement, and sand at 0.45:1:1. Additionally, the reinforcement of the element anchor specimen used an HRB400 steel bar, which was connected to a load cell for monitoring the pullout force. The element anchor specimen had a bond length of 10 cm, which remained constant in pullout loading using a reserved anchor body of 4 cm (Fig. 3).

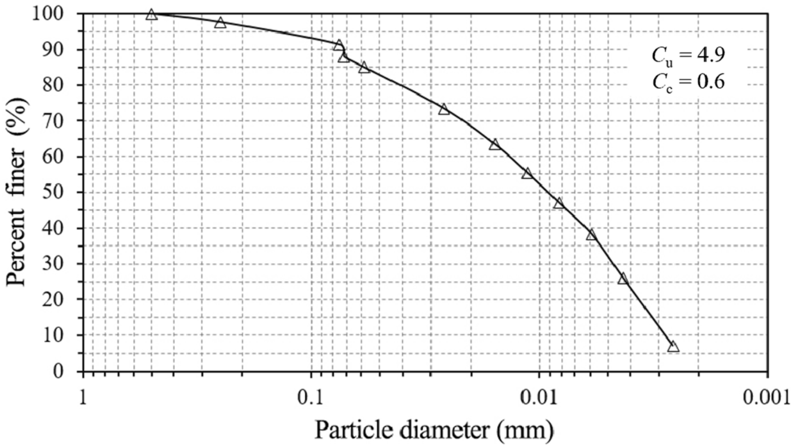

Fig. 1. Particle size distribution of the clayey soil sample.

Table 2
Moisture conditions of the clayey soil for preparing the element anchor specimens.

Testing group number	Target w, %	Actual w (S_r), %	
		Rapid pullout	Creep pullout
CT01	18	17.0(42.6)	17.1(42.9)
CT02	18	17.9(44.9)	17.5(43.9)
CT03	18	18.7(46.9)	18.1(45.4)
CT04	20	19.4(48.6)	19.4(48.6)
CT05	20	20.5(51.4)	20.1(50.4)
CT06	20	20.6(51.6)	19.6(49.1)
CT07	22	22.0(55.2)	22.4(56.2)
CT08	22	22.6(56.7)	22.6(56.7)
CT09	24	23.5(58.9)	23.3(58.4)
CT10	24	24.7(61.9)	25.0(62.7)
CT11	28	27.5(68.9)	28.1(70.5)
CT12	28	28.7(72.1)	29.3(73.5)
CT13	30	30.0(75.2)	29.2(73.2)
CT14	32	32.2(80.7)	32.1(80.5)
CT15	36	35.8(89.8)	35.6(89.3)
CT16	36	36.3(91.0)	35.9(90.0)
CT17	36	36.5(91.5)	37.4(93.8)
CT18	38	37.7(94.5)	39.9(100.0)

Mixture design

The moisture condition of the clayey soil was designed as the main testing variable in the interface creep characterization using pullout test on the element anchor specimen. The saturation degree was used to scale the moisture condition by considering both the moisture content and the void ratio, as formulated:

$$S_r = \frac{G_s w}{e} \tag{1}$$

$$\rho_d = \frac{G_s}{1+e} \tag{2}$$

where S_r indicates the saturation degree of the soil; G_s represents the specific gravity of the soil; w denotes the moisture content of the soil; e is the void ratio of the soil; ρ_d is the dry density of the soil. Furthermore, the relationship between w and S_r can be rewritten as follows:

$$S_r = \frac{G_s \rho_d}{G_s - \rho_d} w \tag{3}$$

Since the value of G_s for the same soil is constant; the dry density ρ_d of the soil was specially controlled to remain unchanged at 1.3 g/cm^3 in preparing the element anchor specimens; the stepwise increasing level for the moisture content and the saturation degree of the clayey soil sample was altered as shown in Table 2.

Preparation of the element anchor specimen

The clayey soil samples were first dried and then watered until they reached a reference moisture content of 20 %. Furthermore, the target dry density of the clayey soil for the element anchor specimen was controlled by weighing a specific mass of dry clayey soil sample with the target moisture content. To check the controlling effectiveness of the moisture condition of the clayey soil, the moisture content was measured using the soil sample obtained by smashing each element anchor specimen when the pullout test was completed. Table 2 displays the number of element anchor specimens, their corresponding target, and actual moisture condition (i.e., the moisture content and the saturation degree). A total of 18 groups of element anchor specimens were prepared in this testing program. Each group contains two parallel specimens, which were used in the rapid pullout test and the creep pullout test respectively. It can be observed in Table 2 that the difference between the target and actual moisture content was less than 1 %, which validates the consistency of the moisture condition of the specimen throughout the pullout tests for interface creep characterization.

The element anchor specimen was prepared using the layered compaction method [22,23]. As depicted in Fig. 2a, the clayey soil sample was weighed and placed into a cylinder in seven layers; the specimen was evenly compacted before the guide rod was removed, leaving a reserved anchor hole. As depicted in Fig. 2b, the anchor hole was gravity grouted using the mortar at a water-cement ratio of 0.45, combined with vibration using thin iron wire to improve the compactness. After the grouting, the specimen was cured in a sealed bag for 28 days to reach a uniform distribution of moisture condition over the entire specimen with the hardened grout (Fig. 3a). After the curing, the soil with a 4 cm height adjacent to the base of the tip of the anchorage was removed. This resulted in the formation of a reserved anchorage body, ensuring a constant interface shearing area throughout the pullout test (Fig. 3b). To mitigate the loss of moisture content of the clayey soil sample during the pullout tests, the gap between the anchorage body and upper cover plate of the compacting cell was sealed with Vaseline (Fig. 3c). Hence, an element anchor specimen with a height of 14 cm, a diameter of 22 cm, and an anchor hole with a diameter of 3.8 cm was prepared as shown in Fig. 3d.

Pullout test

The short-term (rapid) pullout test was performed using the specially designed frictional performance test system [22] to evaluate the ultimate interface shear strength of the element anchor specimen (Fig. 4a). The step rate was set to 1 mm/min, and the real-time moving distance

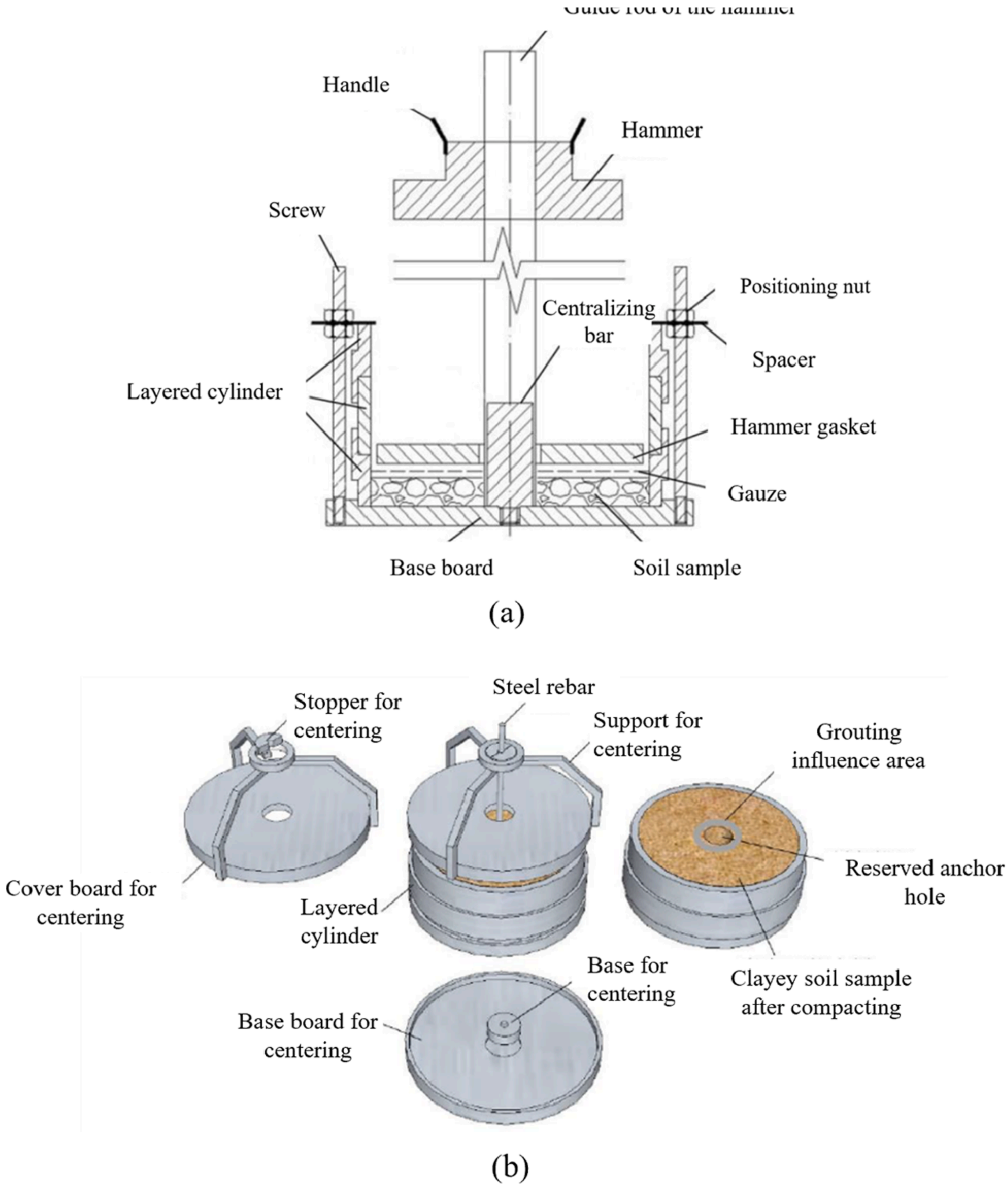

Fig. 2. Schematic diagram of the specially designed device for preparing the element anchor specimen: (a) the compaction device; (b) the grouting device.

was recorded. A load cell was installed connecting to the head of the reinforcement to monitor the real-time pullout force during the loading process. The interface shear stress-displacement relationship was then established based on the idea of an element test that assumes the interface shear stress is uniformly distributed over the entire bond area of the element anchor specimen [13,23].

Meanwhile, the long-term (creep) pullout test was conducted using a specially designed test setup (Fig. 4b). The stepwise loading methodology, which involved applying progressive loadings to each specimen, was adopted. The ultimate pullout resistance obtained from the short-term pullout test was used as a reference for the stepwise loading long-term experiments to avoid interface shear failure. During the long-term procedure, a load ranging from 0.1 to 0.2 N was initially applied, and then another step from 0.10 to 0.15 N was repeatedly applied to ensure sufficient loading effect until the interface creep failed. The specific evolution of loading level (the rate of the load over the ultimate pullout resistance for each single group of element anchor specimens) can be seen in Appendix A. The displacement of the anchorage head for each loading level was recorded using a linear variable differential transformer (LVDT). Specifically, if the anchor head displacement rate dropped below 0.01 mm over 24 h at each loading stage, the following loading step would be added.

Test results

Effect of moisture content on rapid pullout response

The pullout responses monitored in the short-term pullout tests depict the relationship between the interface shear stress and the interface displacement (Fig. 5). All the response curves peak before the

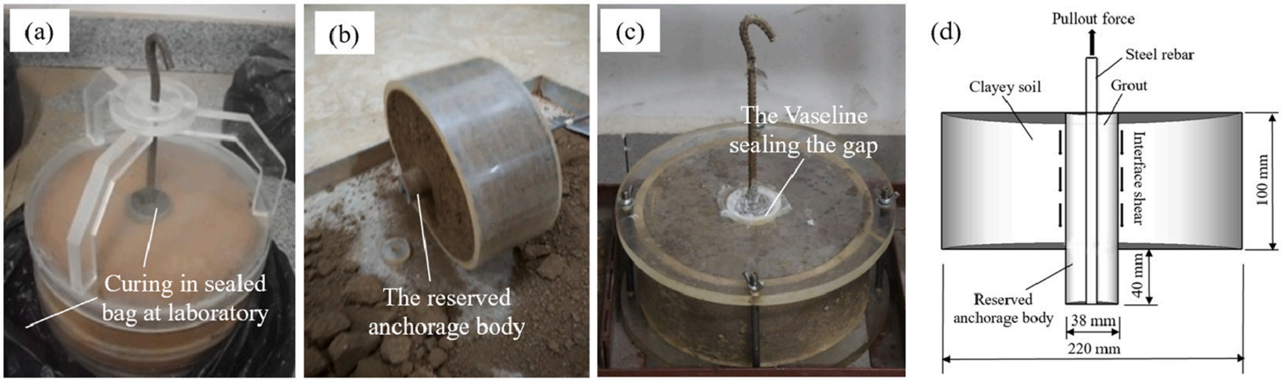

Fig. 3. The key aspects in preparing the element anchor specimen: (a) the specimen cured in a sealed bag to reach uniform distribution of moisture condition over the entire specimen; (b) the reserved anchorage body ensuring constant interface shear area; (c) the sealing process ensuring the consistent moisture condition; (d) the dimension of the element anchor specimen.

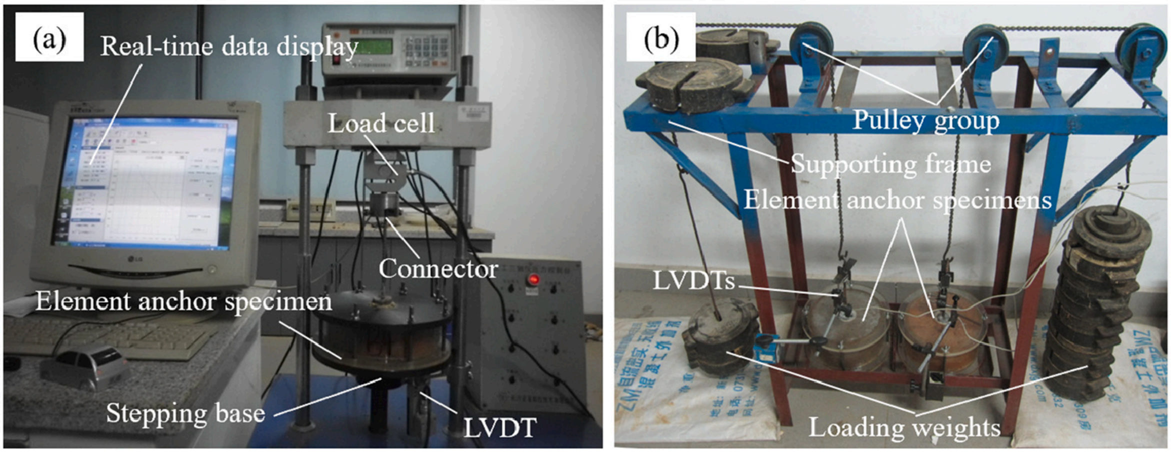

Fig. 4. Pullout test devices for (a) the rapid pullout test; and (b) the creep pullout test.

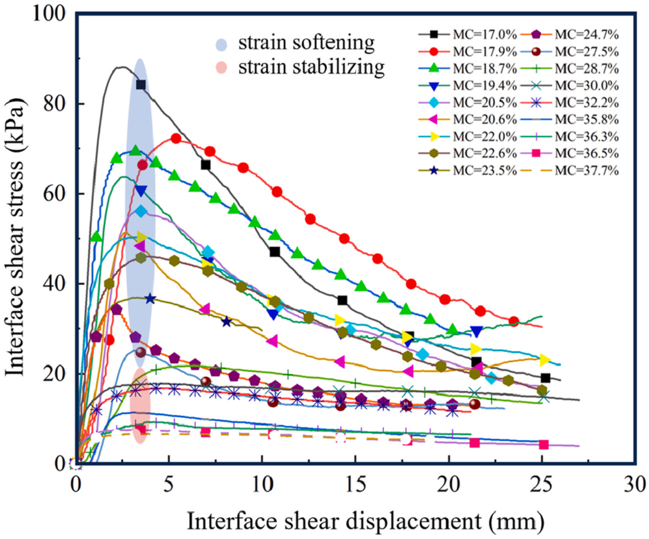

Fig. 5. Interface shear stress-displacement relationship obtained from short-term pullout tests.

displacement reaches 7.5 mm, and then gradually decrease as the displacement increases. For the post-peak behavior, it is interesting to find a threshold of moisture content of the soil near 28.7 %. The curves corresponding to the moisture content below the threshold exhibit the stabilized interface shear stress, while other curves with the moisture content above the threshold manifest obvious decreasing interface shear stress (the strain-softening behavior). Additionally, the strain-softening behavior tends to be more pronounced with the increasing moisture

Table 3
Ultimate and long-term interface shear strength versus the moisture content of the soil.

The moisture content of the soil w (%)	Ultimate interface shear strength τ_u (kPa)	Long-term interface shear strength τ_L (kPa)
17.0	88.00	50.8
17.9	72.33	44.3
18.7	69.56	41.2
19.4	63.69	27.8
20.5	56.15	25.6
20.6	51.46	24.6
22.0	50.28	23.4
22.6	46.09	23.2
23.5	36.88	22.5
24.7	34.36	19.8
27.5	25.14	17.2
28.7	21.79	12.5
30.0	17.85	12.2
32.2	16.76	9.7
35.8	11.40	4.9
36.3	9.22	4.8
36.5	7.54	3.2
37.7	6.70	2.9

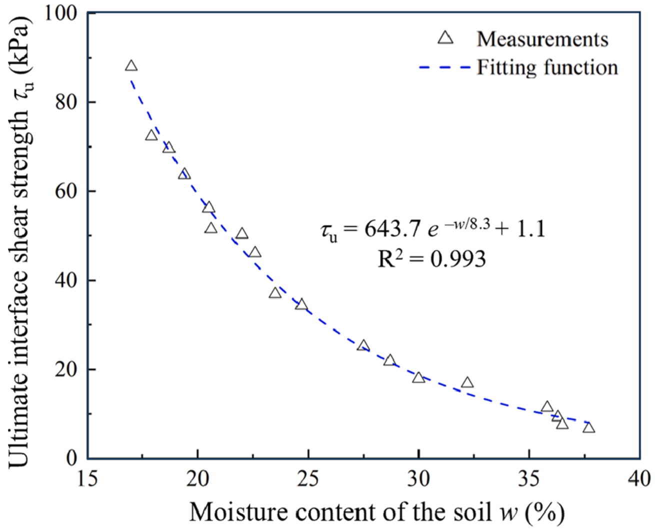

Fig. 6. Ultimate interface shear strength versus moisture content.

content. It is recommended to monitor the moisture change of the soil for the grouted soil anchor in practice, aiming to avoid the excessive displacement of the anchor due to the switch from strain-stabilizing to strain-softening behavior.

The peak of interface shear stress for each curve (Fig. 5) is defined as the ultimate interface shear strength shown in Table 3. The correlation of ultimate interface shear strength and the moisture content of the soil was illustrated in Fig. 6. It can be found that the ultimate shear strength decreases exponentially with the increasing moisture content of the soil; moreover, the moisture-increase-induced degradation of the ultimate interface shear strength develops at large in the range below the abovementioned threshold of moisture content near 28.7 %.

Effect of moisture content on creep pullout response

The time history curve of interface shear displacement for element anchor specimen under stepwise pullout loads is shown in Appendix A. The time history curve under stepwise loads was transformed into a cluster of creep curves corresponding to each single loading level based on a nonlinear superposition method [32], as shown in Appendix B.

The relationship between the time-history curve (Appendix A) and the creep curve (Appendix B) was typically illustrated using the element anchor specimen with a moisture content of 19.4 % (Fig. 7). It can be found that only the creep curve under interface shear stress greater than the long-term interface shear strength was manifested by the full-process of creep phases (including the primary, steady, and accelerated phases). The creep curves under interface shear stress less than the long-term interface shear strength were manifested by the primary and steady phases.

The isochrone curve method [33,34] was used to convert the cluster of interface shear creep curves into a family of interface stress-displacement curves at a specific time, as shown in Appendix C. For each isochronous curve, the existence of an inflection point showing the transition from elastic to elastoplastic behavior was adopted to identify the onset of interface creep damage. The loci defined by the inflection points on different isochronous curves in the interface shear stress–displacement space tend to correspond to a constant stress value. This constant stress is adopted as the long-term interface shear strength.

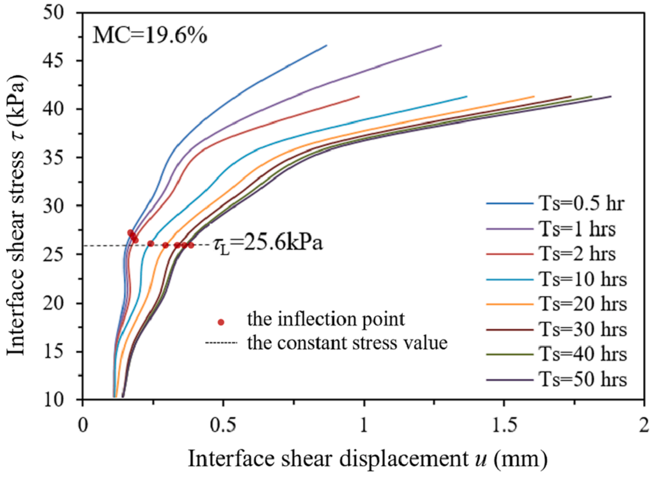

Fig. 8. Typical illustration for the use of the isochrone curve method.

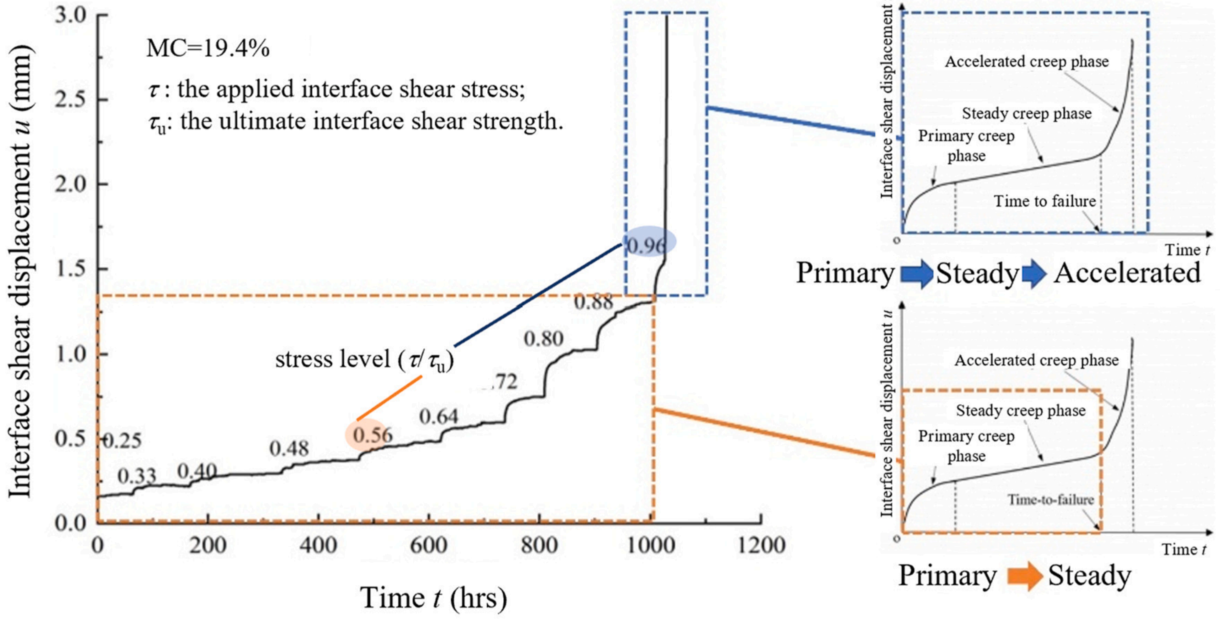

Fig. 7. Typical illustration for creep phases of creep curves under different stress levels.

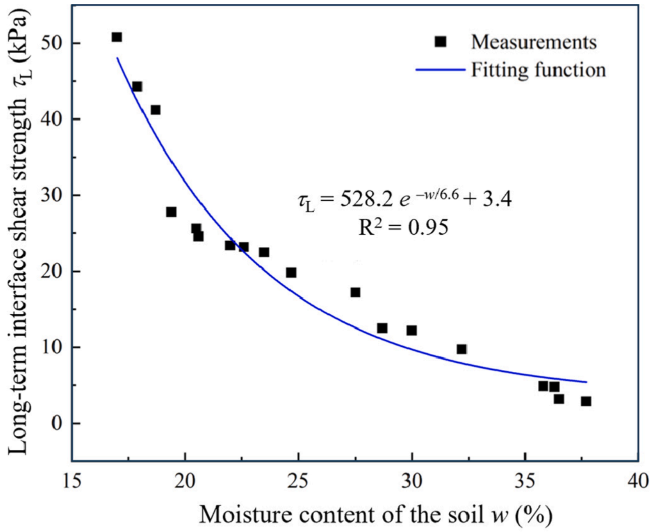

Fig. 9. Long-term interface shear strength versus moisture content of the soil.

The use of the isochrone curve method was typically illustrated in Fig. 8 for the specimen with a moisture content of 19.6 %.

The long-term interface shear strength for element anchor specimens with varying moisture contents of the soil is presented in Table 3. Fig. 9 illustrates that the long-term interface shear strength decreases exponentially over the increasing moisture content, and the moisture content range below the threshold near 28.7 % witnesses the main degradation of the long-term interface shear strength, revealing a similar moisture-increase-induced degrading pattern to that of the ultimate interface shear strength (Fig. 6). The long-term interface shear performance is also analyzed using machine learning methods, which will be systematically examined in the next chapter.

Machine learning models

The methodology adopted for predicting interface creep behavior of grouted soil anchors based on the proposed data-driven approach is depicted in Fig. 10. This included three steps: data acquisition, data-driven model training, and data-driven model validation. Based on the dataset obtained from the creep pullout tests, two ML models and three baseline models were established with the hyperparameters tuned by BAS algorithm. Five evaluation indexes were applied for model validation and Partial Dependence Plot (PDP) was utilized for model

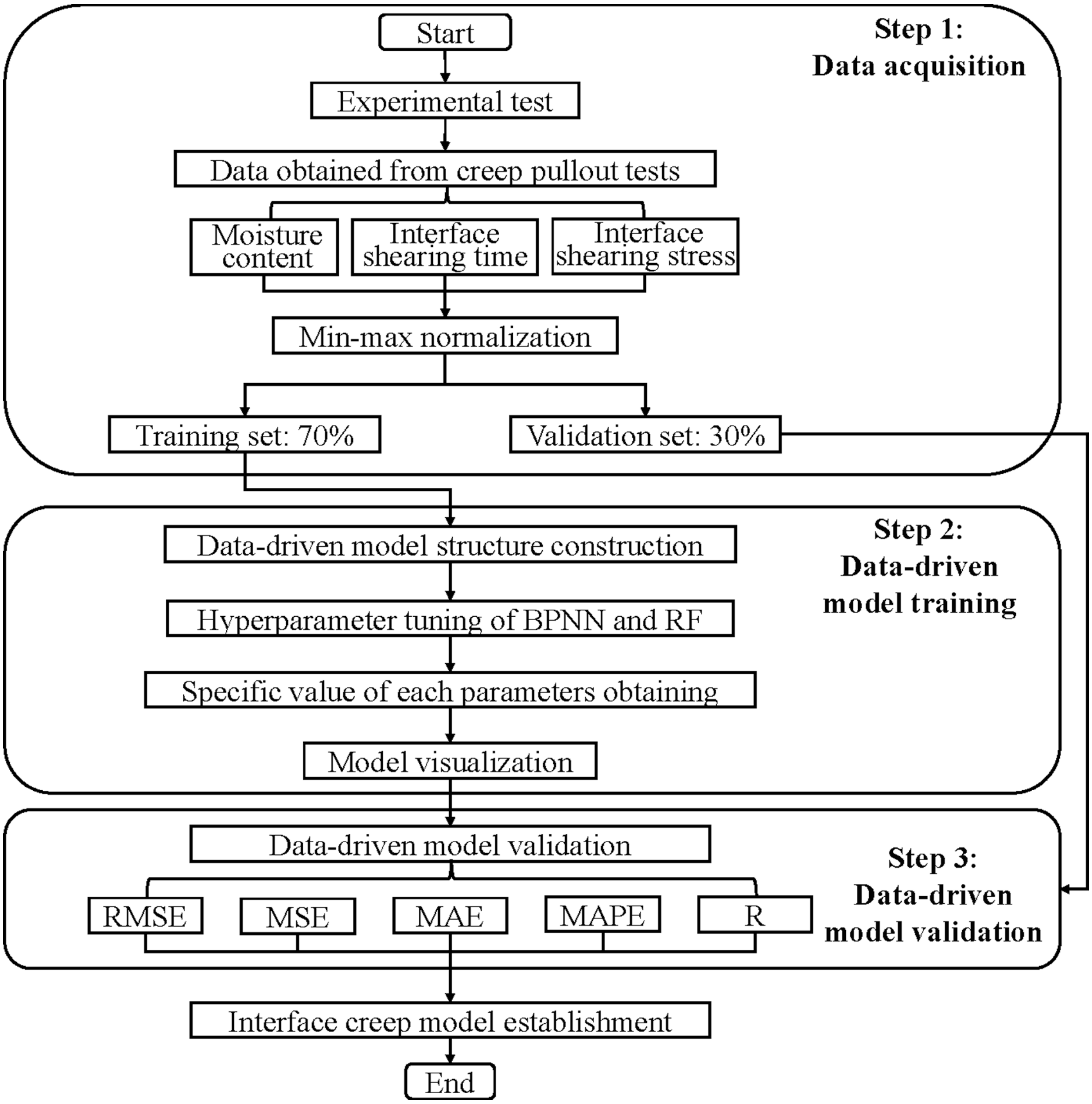

Fig. 10. Implementation flowchart for the adopted methodology.

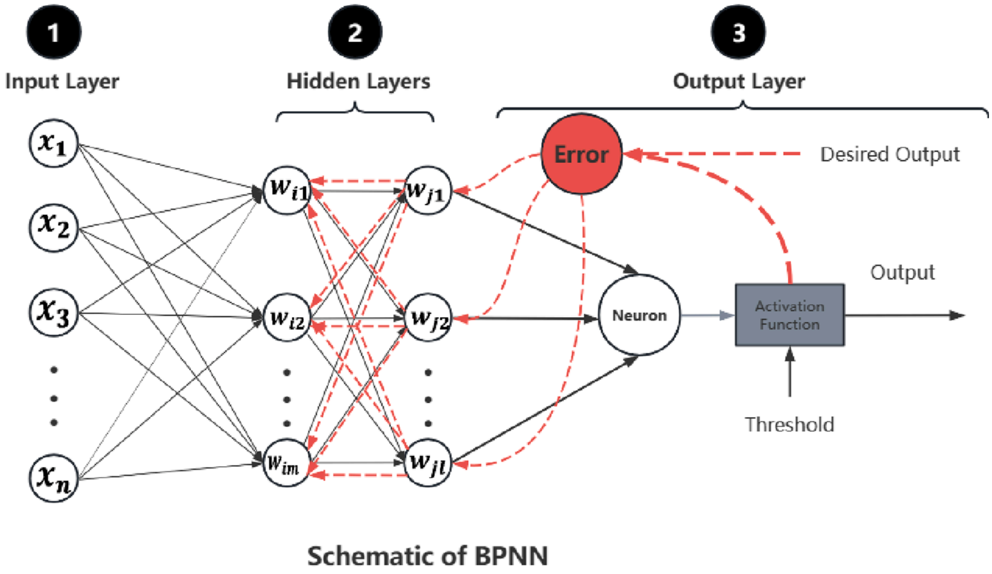

Fig. 11. Algorithm structure of the BPNN.

visualization. The detailed descriptions are introduced in the following subsections.

Data acquisition

As previously stated in describing the experimental program, the moisture content of the soil (w), the interface shearing time (T_s), and the interface shearing stress (τ) were designed as variables in the creep pullout test. The database consisted of 936 data points (18 groups of experimental results), which met the requirement for the database size in traditional machine learning tasks. The machine learning process involved using the moisture content of the soil (w), the interface shearing time (T_s), and the interface shearing stress (τ) as features, and the interface shearing displacement (u) as the output. Due to the differing units and ranges of multiple input and output parameters, parameters with larger values could disproportionately influence the model's performance. To mitigate this potential bias, the experimental dataset results were pre-processed using min–max normalization. This technique scaled all parameter ranges to [0, 1] by applying the following equation.

$$x' = \frac{x - x_{min}}{x_{max} - x_{min}} \tag{4}$$

where the scaled value of the variable x is denoted by x'. The maximum and minimum values of the variable x are, respectively, denoted by x_{max} and x_{min}.

Back propagation neural network (BPNN)

Artificial neural network (ANN) was employed for modeling the relationships between inputs (influencing features) and outputs (i.e. u) [35]. These networks can model the functional relationships between inputs and outputs through their interconnected neurons. Each neuron functions as a computational unit, represented by the following equation:

$$y = max\left(0, \sum_i \boldsymbol{w}_i \boldsymbol{x}_i + b\right) \tag{5}$$

where y and $\boldsymbol{x}_i$ are output and input values of each neuron, respectively; $\boldsymbol{w}_i$ denotes the connection weight; b represents bias value.

Therefore, the output (O) of a neuron is computed by introducing the activation function, which is represented as follows:

$$\mathrm{O} = \mathrm{f}\left(\sum_{i=1}^{n} (\boldsymbol{w}_i \boldsymbol{x}_i) + b\right) \tag{6}$$

$$\mathrm{f}(\mathrm{x}) = \frac{2}{1 + \exp(-\mathrm{x})} - 1 \tag{7}$$

A multilayer network consists of an input layer, an output layer, and multiple hidden layers. In this architecture, the output of each layer serves as the input for the subsequent layer. A standard ANN structure is illustrated in Fig. 11. The BPNN is among the most versatile and widely used types of ANN due to its superior training efficiency. Back propagation serves as an alternative training algorithm that optimizes ANN performance [36–38]. The mean square error (MSE) between the predicted and actual outputs is minimized during this optimization process. Fig. 11 depicts the fundamental principle of BP, which employs the steepest gradient descent method, where the weights are adjusted in the direction of the error gradient, as described by the following equation:

$$\Delta \boldsymbol{w}_n = \alpha \Delta \boldsymbol{w}_{n-1} - \eta \frac{\partial E}{\partial \boldsymbol{w}} \tag{8}$$

where $\boldsymbol{w}$ represents the weight between two neurons; $\Delta \boldsymbol{w}_n$ and $\Delta \boldsymbol{w}_{n-1}$ denote the weight changes at iterations n and n-1, respectively; α and η refer to the momentum factor and learning rate, respectively.

Among the parameters influencing the BPNN structure, the connection weights, bias values, number of hidden layers, and number of neurons per layer have a direct impact on BPNN performance [39]. The convergence speed is contingent upon the initialization of the connection weights and bias values. The complexity of the BPNN architecture is determined by the number of hidden layers and the number of neurons in each hidden layer, which are often addressed through trial-and-error methods. This study employed the BAS algorithm to fine-tune these parameters (i.e., the number of hidden layers and neurons per layer) for optimizing the BPNN architecture.

Random forest (RF)

RF exerts the ensemble learning method in revealing the relationship between features and results and then generates stable and accurate results as predictions. Specifically, the bagging algorithm embedded in RF divided variables into large numbers of decision trees (RTs) as the base classifier [40,41]. The ultimate output will be computed by

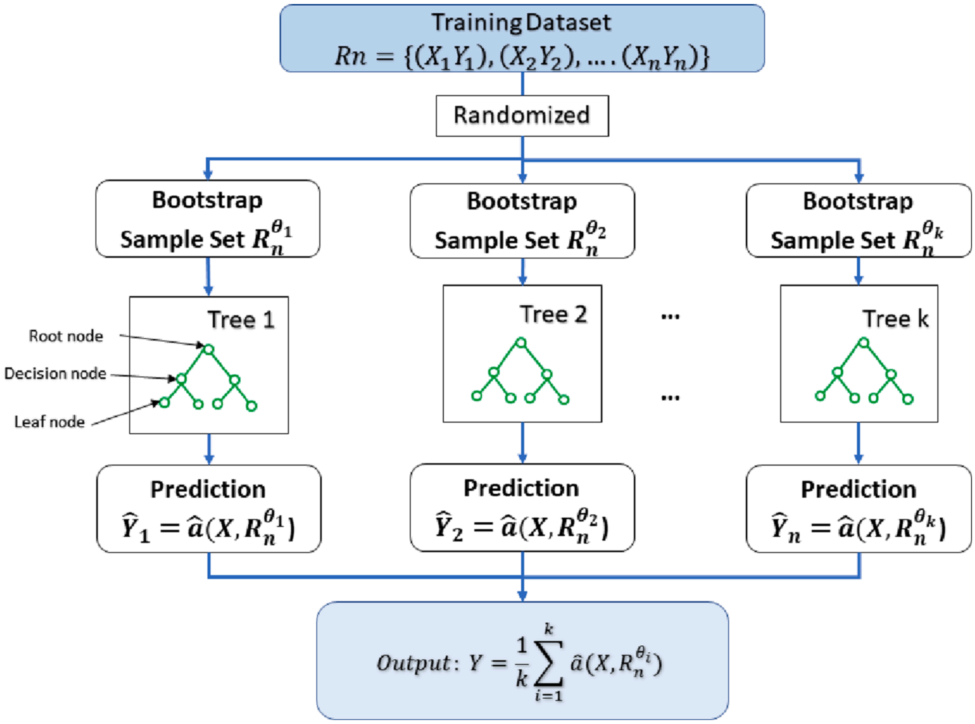

Fig. 12. Construction of an RF model.

averaging the further voting result on RTs [42]. In the training set R_n, X is the input vector containing m independent variables ($X = \{x_1, x_2, \cdots, x_m\}$), while Y is the output scalar. In this study, R_n denotes the experiment datasets with X representing the input vector consisting of three features and Y representing the output (u). Each sample within the training set undergoes evaluation by decision nodes using a specified split function.

During the training of each RT, a subset of n samples is randomly drawn from the training set R_n without replacement. This process, referred to as 'bootstrap' results in the formation of a new sample set R_n^{θ}. The training then proceeds by splitting the samples in R_n^{θ} from the root node to the leaf nodes, with each node utilizing its own split function. At the conclusion of this training phase, the prediction function $\widehat{a}(X, R_n^{\theta})$ is established based on the dataset R_n^{θ}. RF aggregates the results from each individual RTs and uses the average of these results as the final output. As illustrated in Fig. 12, the RF algorithm consists of k de-correlated RTs, resulting in k prediction functions $\widehat{a}(X, R_n^{\theta_k})$, where k $k = 1, 2, \cdots, k$. The symbol θ_k represents an independently distributed random vector corresponding to different RTs. Ultimately, the RF generates k outputs $\{\widehat{Y}_1, \widehat{Y}_2, \cdots, \widehat{Y}_k\}$ for each RT. The final prediction Y is obtained by averaging these outputs, as depicted in Eq. (10).

$$R_n = \{(X_1, Y_1), (X_2, Y_2), \cdots, (X_n, Y_n)\}, X \in \mathbb{R}^m, Y \in \mathbb{R}. \tag{9}$$

Baseline models

Existed models such as logical regression (LR), multiple linear regression (MLR), and K-Nearest Neighbor (KNN) are usually employed as baseline models to assess the software effort of the newly proposed models [43–45]. Specifically, the characteristic of regression models (LR and MLR) on minimum computation and easy implementation facilitates relationship identification between predictor and output. Equations (11) and (12) display the principles of LR and MLR models.

$$ln\frac{p}{1-p} = b_0 + \sum_{k=1}^{n} b_k x_k \tag{11}$$

$$Y = \beta_0 + \beta_1 x_1 + \beta_1 x_2 + \cdots + \beta_n x_n \tag{12}$$

where x_k denotes the independent variable; p represents the dependent variable; b_0 and b_k are constant coefficients; Y denotes the output; $x_1, x_2, \cdots, x_n$ denote the multiple predictive variables; $\beta_1, \cdots, \beta_n$ denote the regression coefficients.

The KNN model detects the nearest neighbors of the target input and then averages the corresponding results of neighbors as the ultimate prediction [46]. The same weight is set for all neighbors (y_i and y_j) and the distance of the dataset is calculated by Equation (13).

$$\mathrm{d(i,j)} = \sqrt{\left(y_{i1} - y_{j1}\right)^2 + \left(y_{i2} - y_{j2}\right)^2 + \text{Â·Â·Â·} + \left(y_{in} - y_{jn}\right)^2} \tag{13}$$

where i and j represent the detected points and d is the abbreviation of Euclidean distance.

Beetle antennae search (BAS)

Meta-heuristic algorithms have been adopted in tuning hyperparameters when applying ML models for optimization problems [47,48]. The optimal functions of BAS simulate the behavior when beetles forage and the flowchart is shown in Fig. 13. Specifically, the BAS algorithm exhibits a positive effect on tuning the optimal hyperparameters, and the pseudocode is presented in Fig. 14. Specifically, the beetle uses its two antennae to detect odor concentration and moves toward the direction where the concentration is strongest. Based on this insight, the positions of the left and right antennae are used to represent the values of all hyperparameter combinations (e.g., the number of hidden layers and neurons in each layer for BPNN), denoted as the x_l^i and x_r^i with superscript i illustrating the i^{th} iteration. The odor concentration is determined by calculating the value of the objective function which is Root-mean-square error (RMSE). After determining the RMSE values of x_l^i and x_r^i, the beetle will move to the next position and update its antennae position to $x_l^{(i+1)}$ and $x_r^{(i+1)}$. This process aims to reduce the RMSE values and finally obtain the best hyperparameter combinations

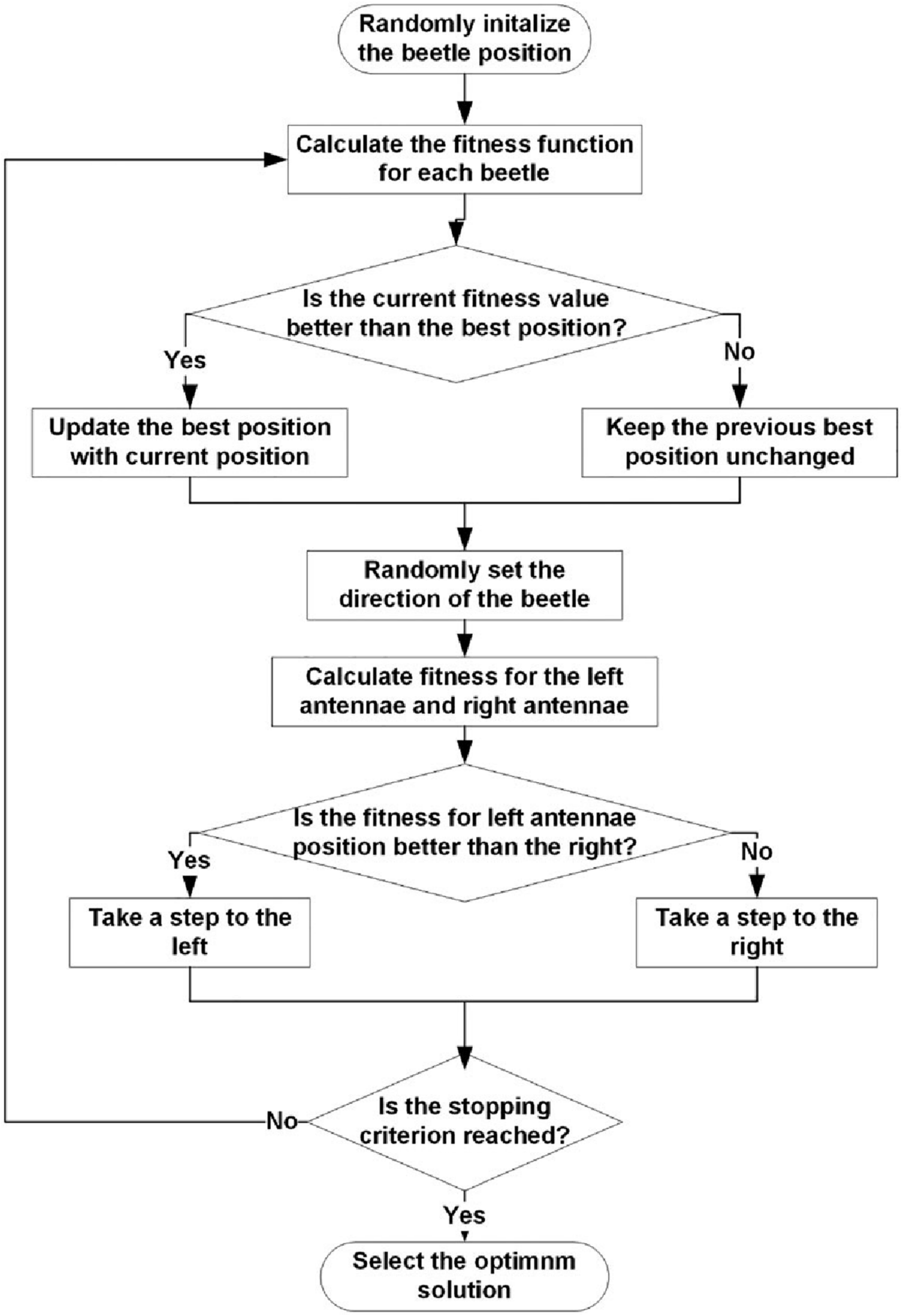

Fig. 13. Flowchart of BAS [49].

corresponding to the minimum RMSE value. Based on this theory, the mathematical expressions are as follows:

Equation (14–15) can be used to calculate the location of the left and right antennae.

$$\mathbf{x}_r^i = \mathbf{x}^i + d^i\mathbf{b} \tag{14}$$

$$\mathbf{x}_l^i = \mathbf{x}^i - d^i\mathbf{b} \tag{15}$$

where $\mathbf{x}_r^i$ and $\mathbf{x}_l^i$ represent the left and right antennae directions, respectively; $\mathbf{x}^{\mathbf{i}}$ is the beetle position at an i^{th} iteration. d^{i} denotes the length of the beetle's antennae at i^{th} iteration. **b** presents a random normalized unit vector expressed as follows:

$$\mathrm{b} = \frac{\mathrm{rnd}(\mathrm{k},1)}{\|\mathrm{rnd}(\mathrm{k},1)\|} \tag{16}$$

where k denotes the position dimensionality; $\mathrm{rnd}(\hat{\mathrm{A}}\cdot)$ is a random function

The beetle's position will be updated based on the following equation:

$$\mathbf{x}^{i+1} = \mathbf{x}^i + \delta^i\mathbf{b}\hat{\mathrm{A}}\cdot\mathrm{sign}(f(\mathbf{x}_r) - f(\mathbf{x}_l)) \tag{17}$$

where $\mathrm{sign}(\hat{\mathrm{A}}\cdot)$ indicates the sign function; $f(\mathbf{x}_r)$ and $f(\mathbf{x}_l)$ are the RMSE values of x_l^i and x_r^i; δ^{i} represents the step size at the i^{th} iteration, which is updated using the following formula:

$$\delta^{i+1} = \eta\delta^i \tag{18}$$

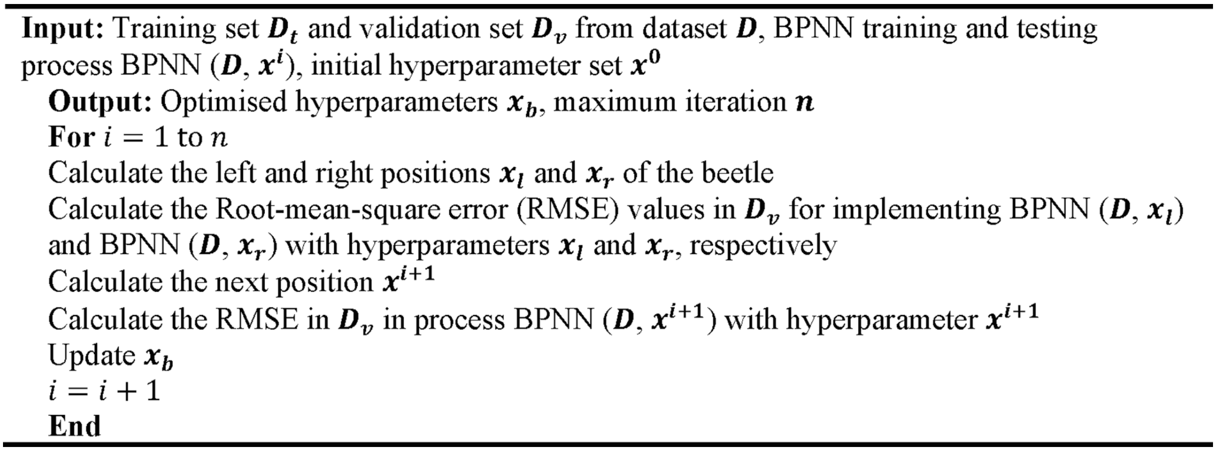

```
Input: Training set $D_t$ and validation set $D_v$ from dataset $D$, BPNN training and testing
process BPNN ($D$, $x^i$), initial hyperparameter set $x^0$
  Output: Optimised hyperparameters $x_b$, maximum iteration $n$
  For $i = 1$ to $n$
  Calculate the left and right positions $x_l$ and $x_r$ of the beetle
  Calculate the Root-mean-square error (RMSE) values in $D_v$ for implementing BPNN ($D$, $x_l$)
  and BPNN ($D$, $x_r$) with hyperparameters $x_l$ and $x_r$, respectively
  Calculate the next position $x^{i+1}$
  Calculate the RMSE in $D_v$ in process BPNN ($D$, $x^{i+1}$) with hyperparameter $x^{i+1}$
  Update $x_b$
  $i = i + 1$
  End
```

Fig. 14. The pseudocode of tuning hyperparameters of BPNN using BAS [50].

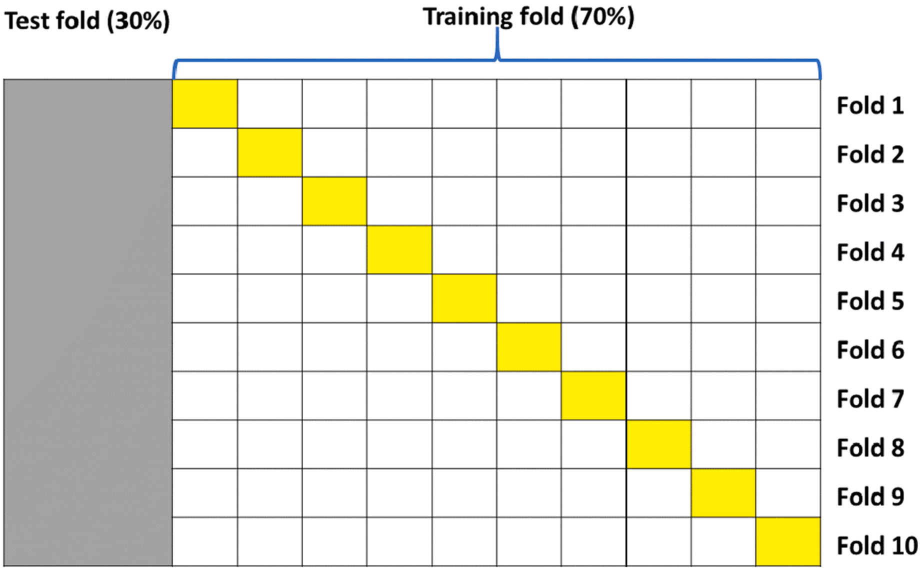

Fig. 15. A ten-fold cross-validation.

where η is the attenuation coefficient of the step size.

Performance evaluation

To tune hyperparameters in the training dataset (Fig. 15), a ten-fold cross-validation (CV) was performed [51,52]. Firstly, 70 % of the original data was randomly selected for the training process and the ten-fold CV, while the remaining dataset was kept aside to assess the model performance. During the training process, each fold was used once to validate the models whose neurons had been adjusted by other folds. The BAS algorithm was used to tune the hyperparameters of the ML models through 50 iterations during the training process. The root mean square error (RMSE) was saved to determine the optimal model structure. This process was repeated 10 times to complete the 10-fold CV. Ultimately, the trained model with the optimal hyperparameters was used for validation of the test set and prediction of the output outcome.

Definitions of the two accuracy evaluation indexes including RMSE, MSE, mean absolute error (MAE), mean absolute percentage error (MAPE), and index correlation coefficient (R) are shown as follows:

$$RMSE = \sqrt{\frac{1}{n}\sum_{i=1}^{n}\left(y_i^* - y_i\right)^2} \tag{19}$$

$$MSE = \frac{1}{n}\sum_{i=1}^{n}\left(y_i^* - y_i\right)^2 \tag{20}$$

$$MAE = \frac{1}{n}\sum_{i=1}^{n}\left|y_i^* - y_i\right| \tag{21}$$

$$MAPE = \frac{1}{n}\sum_{i=1}^{n}\left|\frac{y_i^* - y_i}{y_i}\right| \tag{22}$$

$$R = \frac{\Sigma_{i=1}^{N}\left(y_i^* - \overline{y^*}\right)\left(y_i - \overline{y}\right)}{\sqrt{\Sigma_{i=1}^{N}\left(y_i^* - \overline{y^*}\right)^2}\sqrt{\Sigma_{i=1}^{N}\left(y_i - \overline{y}\right)^2}} \tag{23}$$

where n denotes the data quantity; y_i^* presents the predicted output; y_i is the actual output; both $\overline{y^*}$ and $\overline{y}$ reflect the corresponding mean values.

ML model visualization

The primary aim of utilizing machine learning is to produce decisions based on the model output. The model interpretability is essential in this process to comprehend the underlying processes and outputs of a machine learning model. However, as machine learning is perceived

Table 4
The initial values of hyperparameters of BPNN model.

Number of neuron layers	Neuron number of the 1st layer	Neuron number of the 2nd layer	Neuron number of the 3rd layer
1	20	/	/
2	20	10	/
3	7	4	8

as an opaque "black box," the development of interpretable techniques for model visualization (both locally and globally) is valuable. Partial Dependence Plot (PDP) is one of the global interpretable methods, which represents the impact of one or two features on the model's output. Moreover, PDP can provide a linear, monotonic, or complex relationship between the target and the feature. The technique was originally proposed by Friedman in 2001 where the partial dependency function of regression is shown in Equation (24) [53].

$$f_{xs}(x_s) = E_{xs}[f_{xs}(x_s,x_c)] = \int f_{xs}(x_s,x_c)dP(x_c) \tag{24}$$

where, x_s is the feature and the partial dependency function, f is the established ML model, and x_c is the other features in f. The feature (s) are selected features in the study. The feature vectors x_s and x_c define the whole feature space x. The link between the features in set C and the model output can be established by marginalizing the model output on the feature distribution in set C. A function that solely depends on the features in set S can be obtained by marginalizing other features.

Machine learning prediction results

Hyperparameter tuning of BPNN and RF

Initial hyperparameters of ML models were set before the training process to determine the model structure [54]. The 70 % of the original experimental data was used for model training and the optimal hyperparameters' selection. The remaining data was used to evaluate the accuracy and generalization performance of the trained models. In the training process, the BAS was used to perform a 10-fold CV to tune the hyperparameters, which were determined corresponding to the minimum RMSE. The BAS algorithm ran for 50 iterations in each fold.

During the training process of the BPNN models, the number of hidden layers ranged from 1 to 3, and the initial neuron settings per layer are detailed in Table 4. The learning rate was set at 4.3e-05. With hyperparameters tuned by the BAS algorithm, the optimal configuration was determined to be 2 hidden layers with [6,37] neurons. Fig. 16a depicts the iteration process of the BAS algorithm in the best fold within the 10-fold cross-validation. The BPNN models with 2 hidden layers achieved the lowest RMSE values after 50 BAS iterations, confirming that 2 hidden layers were optimal. Fig. 16b presents the RMSE convergence during the 10-fold CV when using 2 hidden layers. The final fold exhibited the lowest RMSE value, as shown in the iteration process in Fig. 16c. The minimum RMSE for the verification set in the last fold was 0.0818 at the 35th iteration. The blue curve represents the RMSE changes during iterations, while the red curve shows the minimum RMSE throughout the training process. The RMSE stabilizing after 35 iterations indicates that the BAS algorithm effectively tuned the BPNN hyperparameters.

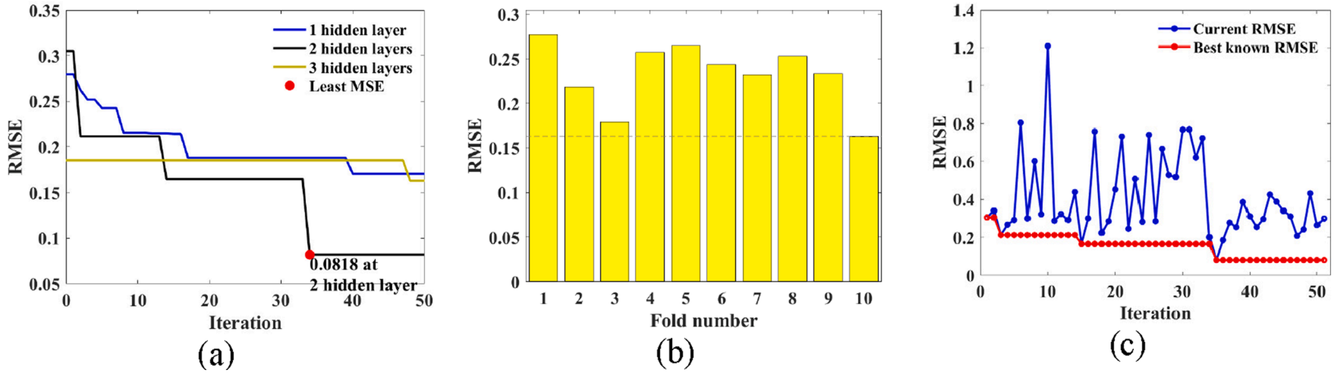

Fig. 16. Hyperparameter tuning for BPNN: (a) RSME iteration with various numbers of hidden layers; (b) RSME values obtained in 10 validation folds; (c) Iteration conducted at the 10th fold.

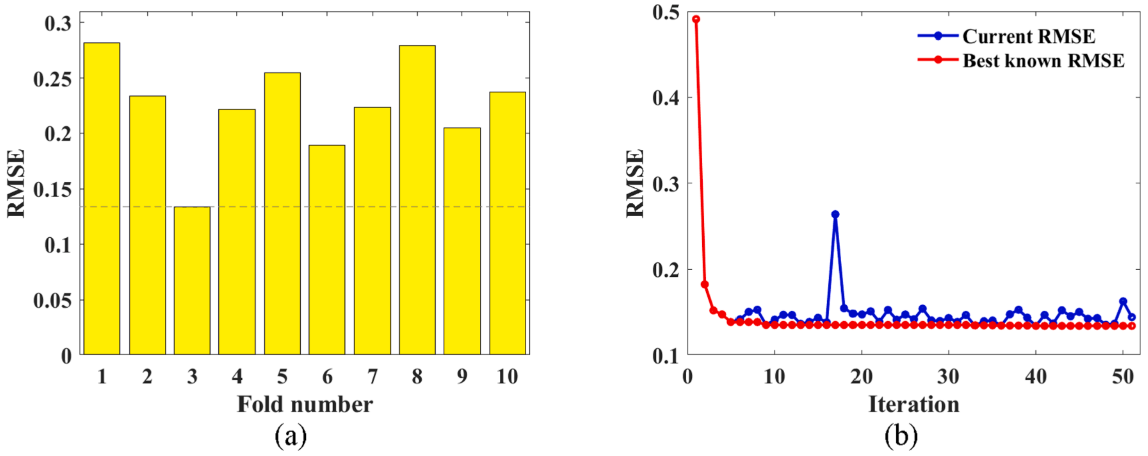

Fig. 17. Hyperparameter tuning for RF: (a) RSME values obtained in 10 validation folds; (b) Iteration conducted at the 3rd fold.

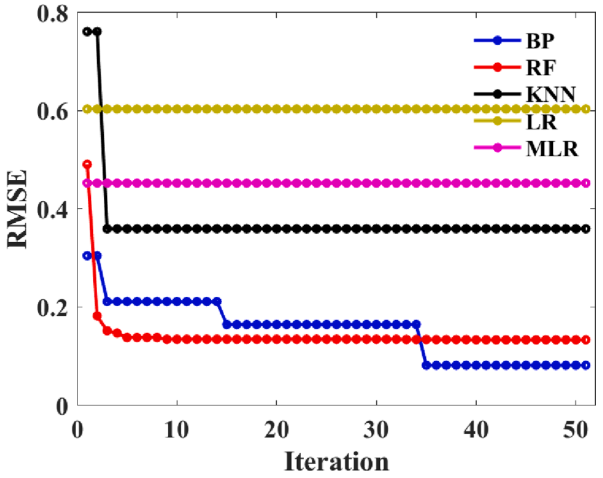

Fig. 18. The RMSE iteration comparison for 5 ML models.

Similarly, the number of trees (*numTreenumTree*) and the minimum number of leaves (*minNumleafminNumleaf*) are critical hyperparameters that were initially set to 40 during the training process of the RF model. Utilizing the BAS algorithm in conjunction with a 10-fold CV, the optimal hyperparameters were determined from the fold with the minimum RMSE. As depicted in Fig. 17a and 17b, the third fold achieved the smallest RMSE, which progressively decreased with each iteration. The RMSE reached its minimum value at the 40th iteration, indicating convergence and effective hyperparameter tuning. Ultimately, the optimal hyperparameters were *minNumleaf* = 1 and *numTree* = 162. Fig. 18 illustrates the RMSE values for the five ML models throughout the training process. The BAS-RF model achieved the lowest RMSE among all models within the first 35 iterations, while the BAS-BPNN model attained the lowest RMSE compared to the other models after 35 iterations.

Performance of BAS-BPNN and BAS-RF for shearing displacement

Fig. 19 and Fig. 20 illustrate the predicted performance of established BAS-BPNN and BAS-RF models, with subfigures (a) and (b)

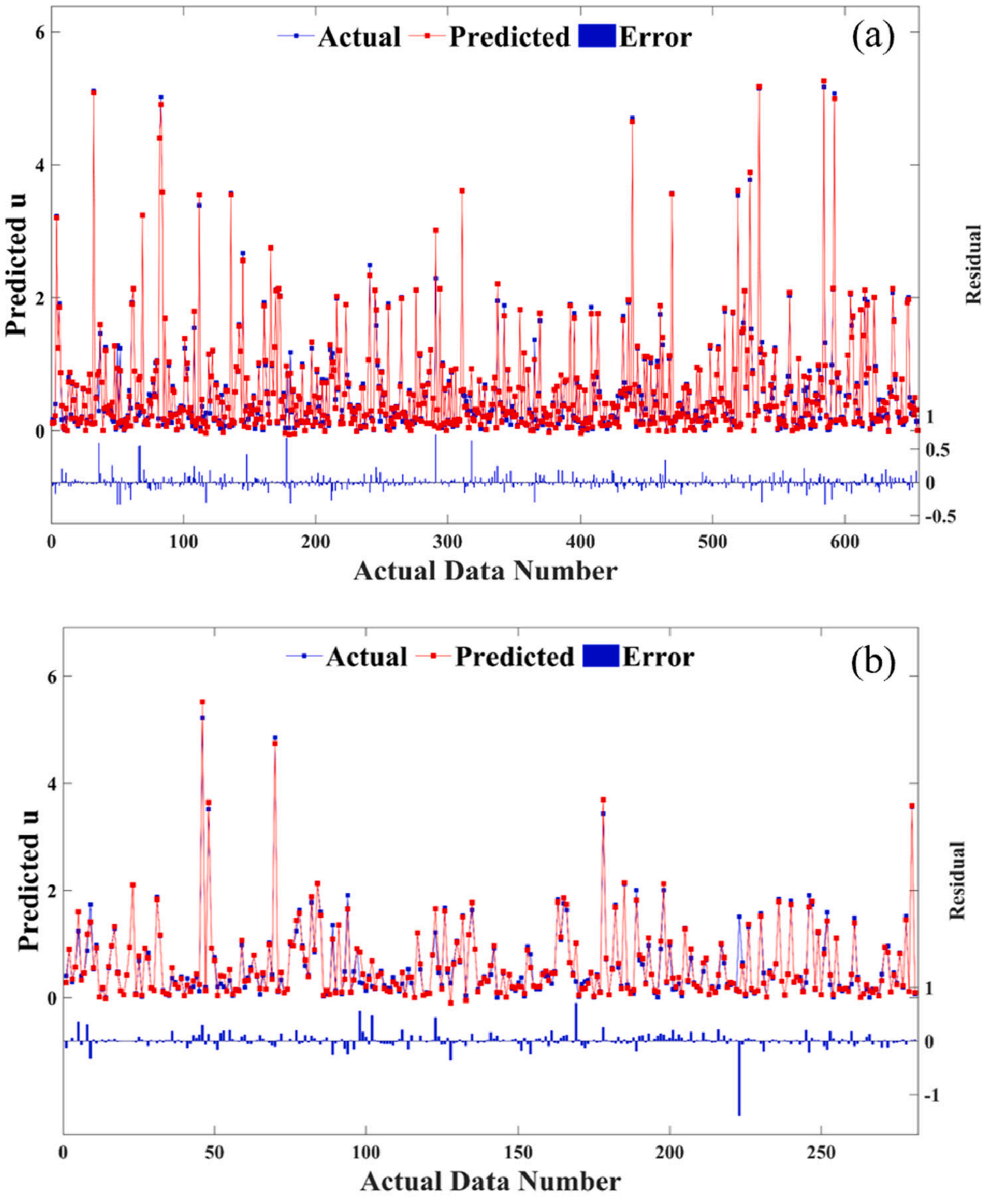

Fig. 19. Difference between actual and predicted *u* on the (a) training group and (b) test group based on BAS-BPNN model.

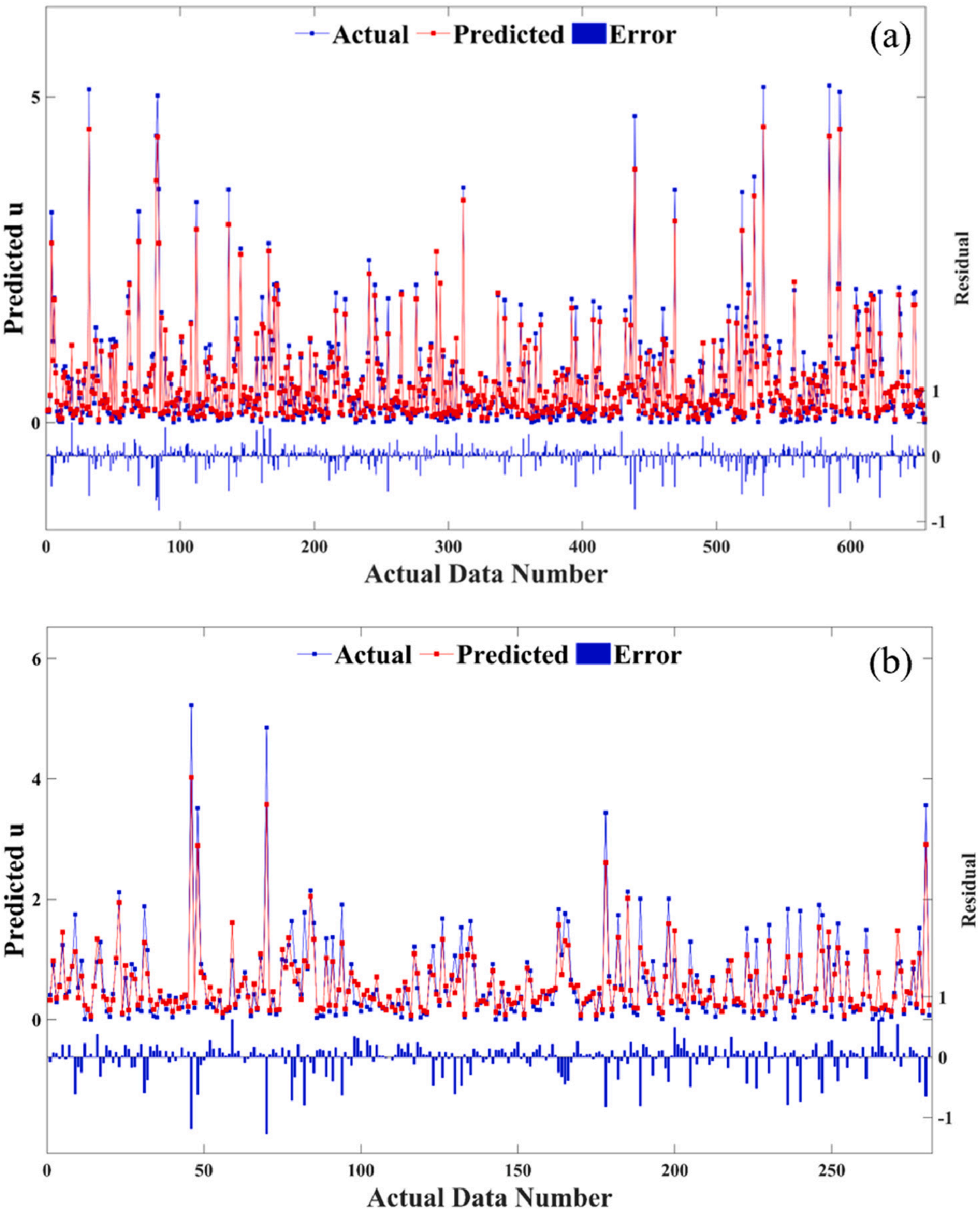

Fig. 20. Difference between actual and predicted *u* on the (a) training group and (b) test group based on BAS-RF model.

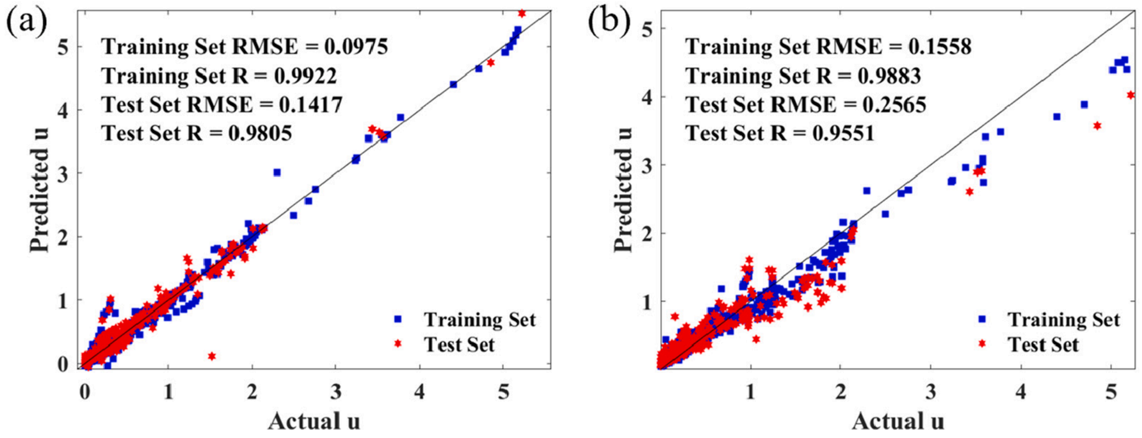

Fig. 21. Scatter plot of predicted and actual shearing displacement of training and test sets: (a) BAS-BPNN model; (b) BAS-RF model.

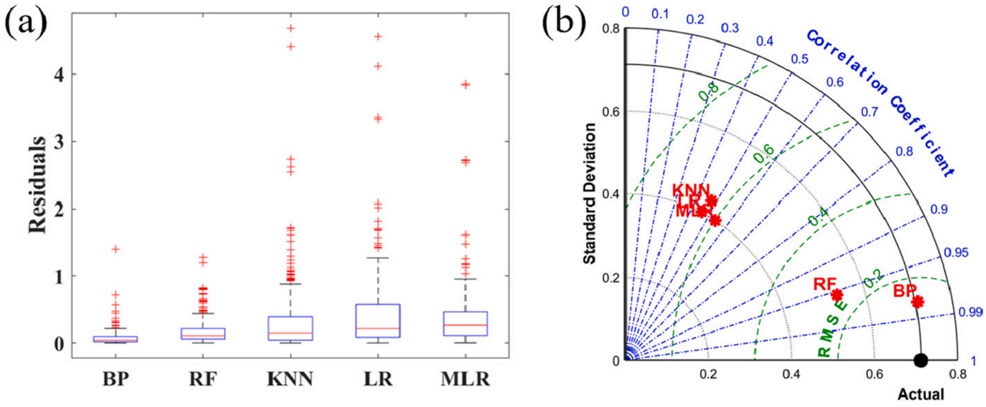

Fig. 22. Performance evaluation of four models by (a) boxplot and (b) Taylor diagram.

Table 5
Evaluation of ML models on the interface creep test.

Evaluation index	Model				
	BPNN	RF	KNN	LR	MLR
MSE	0.0201	0.0658	0.4201	0.5574	0.3592
RMSE	0.1417	0.2565	0.6482	0.7466	0.5993
MAE	0.0755	0.1719	0.3367	0.4357	0.3705
MAPE	0.7051	1.6213	1.2425	0.8925	3.6725
R	0.9805	0.9551	0.4756	0.4561	0.5401

depicting the training and test sets, respectively. The blue points show the actual value and the red points are the predicted value where the overlap of blue and red points illustrate the accuracy and reliability of the model. Compared with RF model, the error between actual and predicted u (bottom blue line) was relatively lower for BPNN model, illustrating the better performance of BPNN. Meanwhile, Fig. 21 depicts the scatter plot of the predicted u via BAS-BPNN and BAS-RF models. The diagonal line illustrates the comparison between the actual and predicted values. The proximity of the data points to the diagonal line serves as an indicator of prediction accuracy. When a data point is close to this line, it signifies a small discrepancy between the actual and predicted values, thereby reflecting the model's precision in forecasting. In the test set of BAS-BPNN, the RMSE and R values were 0.1417 and 0.9805, respectively, while they were 0.2565 and 0.9551 for BAS-RF.

Comparison of BPNN, RF, KNN, LR, and MLR

Fig. 22a presents a box plot comparing the discrepancy between the predictions and actual values across different models, including BPNN, RF, KNN, LR, and MLR. The height of the boxes represents the interquartile range. BPNN exhibited the lowest prediction error compared to the other four algorithms, as evidenced by the interquartile range and median. Despite having multiple outliers in the displacement predictions, BPNN's upper limit of error was lower than that of KNN, LR, and MLR, indicating that BPNN had the highest accuracy among these ML models. Fig. 22b displays a Taylor diagram, which combines three model evaluation metrics—standard deviation, RMSE, and R into polar coordinates. Additionally, Table 5 lists the RMSE and R values used for model evaluation. Points close to the "actual" mark on the Taylor diagram signify better performance in terms of correlation coefficient, RMSE, and standard deviation. Therefore, the BPNN model demonstrated superior performance compared to the other four machine learning models.

Model visualization

The partial dependence plot (PDP) figure visualized the relationship between BPNN predicted long-term displacement u and selected features (moisture content w, interface shear stress τ, and interface shear time T_S), as shown in Fig. 23. The x-axis and y-axis depict the features and the colour map exhibits the value distribution of the shear displacement which is calculated by the BPNN model. This extends the data space from the limited experimental samples to the unlimited samples within the feasible zone.

From Fig. 23a, the moisture content of around 0.37 corresponds to the largest long-term shear displacement, while the high or low moisture contents both reduce the displacement. Regarding T_s, the shear time, it is reasonable that longer shear time results in larger shear displacement. Moreover, the map shows larger effect of moisture content on displacement than that of T_s on displacement. In particular, the time effect on the displacement tends to exhibit a limited range corresponding to different moisture conditions, which means the moisture-change-induced displacement would mainly develop within the time range. The range increases with the increasing moisture content, but not longer than 20 h (i.e., the left bound for the yellow zone of the interface shear displacement in Fig. 23a). It reveals a critical implication that the displacement of grouted soil anchor in practice demands a tight monitoring within the time range of 20 h after the onset of the soil moisture variation. The monitoring beyond the time range would lead to missing out the moisture-change-induced displacement development of the anchor, and result in a wrong evaluation of the in-service performance of the grouted soil anchor.

Fig. 23b and 23c depict another feature, interface shear stress τ, to visualize the interaction influence of τ-T_s and τ-w to the long-term interface shear displacement. The largest long-term interface shear displacement is found in the yellow zone of the figure, corresponding to the largest interface shear stress and moisture content. In addition, it can be observed that shear stress and moisture content have a similar

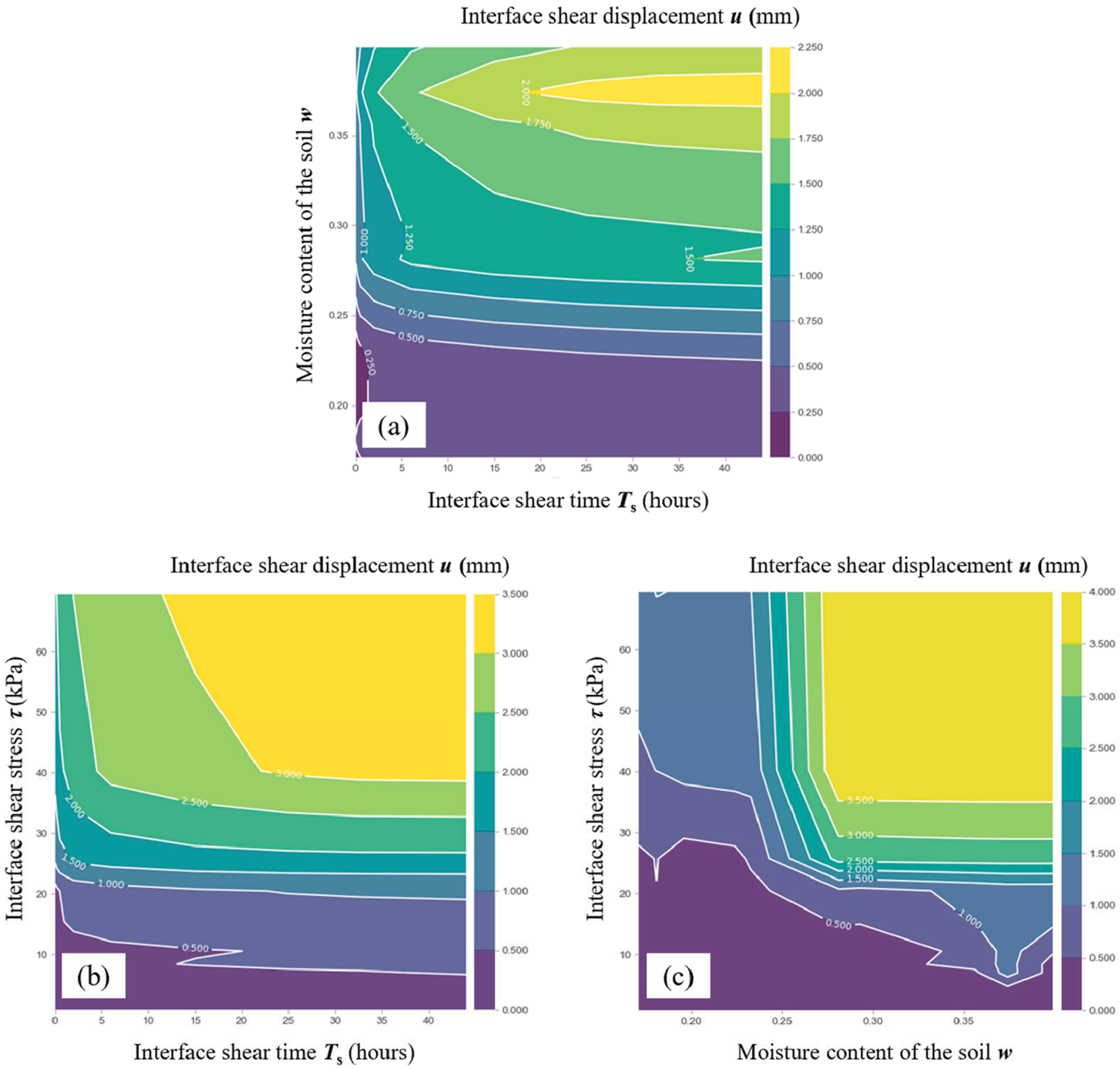

Fig. 23. Visualization of the predicted displacement using PDP: (a) u-w-T_s; (b) u-τ-T_s; (c) u-τ-w.

influence on the long-term shear displacement. It implies that the soil moisture change should be treated as important as the loading change in designing the time-dependent performance of the grouted soil anchor in practice.

Conclusions

This research investigates the coupled effect of soil moisture condition and interface shear stress on the interface shear creep behavior of grouted anchors embedded in clayey soils through laboratory testing and machine learning modeling. The obtained findings can be summarized as follows:

(1) There is a threshold of moisture content near 28.7 %, beyond which the interface shear stress-displacement response would change from strain-stabilizing behavior to strain-softening behavior; the monitoring of the moisture condition of the soil is highly recommended for the grouted soil anchor in practice to avoid the moisture-change-induced displacement development of the anchor.

(2) The ultimate and long-term interface shear strength both decrease exponentially with the increasing moisture content of the soil; the moisture-increase-induced degradation of interface shear strength develops mainly in the range lower than the threshold of moisture content near 28.7 %. The time-dependent behavior of the grouted soil anchor is much more sensitive to the early phase of increasing moisture than the late phase, which demands more concerns in practice.

(3) BPNN showed the highest prediction accuracy in comparison with RF and baseline models (LR, MLR, and KNN) for interface creep behavior of grouted anchors embedded in clayey soils with an MSE of 0.0201, RMSE of 0.1417, MAE of 0.0755, MAPE of 0.7051, and R of 0.9850.

(4) The soil moisture content and interface shear stress demonstrate more important impact to the interface shear displacement than the interface shear time; the moisture-change-induced interface displacement develops mainly with the time range of 20 h after the onset of the moisture change, in which the tight monitoring of displacement of the grouted soil anchor is necessarily demanded in practice.

The above-concluded remarks along with the presented data-driven modeling of interface creep behavior can provide insights into the designing practice and facilitate the necessary evaluation for the long-term in-service performance of the grouted soil anchor experiencing the soil moisture fluctuation in seasoned rainfall conditions. However, the extended application of the above conclusions to the grouted soil anchor embedded in soils other than the clayey soil used in this study is not recommended without enriching data from respective laboratory tests.

CRediT authorship contribution statement

Genbao Zhang: Methodology, Conceptualization. **Changjie Xu:** Methodology, Formal analysis. **Di Wang:** Writing – original draft, Formal analysis. **Yufei Wang:** Writing – original draft, Formal analysis. **Junbo Sun:** Supervision, Conceptualization. **Shimin Zhu:** Methodology, Formal analysis. **Amr M. Morsy:** Methodology, Conceptualization. **Zhonghe Liu:** Writing – review & editing. **Xiangyu Wang:** Supervision, Conceptualization.

Declaration of competing interest

The authors declare that they have no known competing financial interests or personal relationships that could have appeared to influence the work reported in this paper.

Data availability

Data will be made available on request.

Acknowledgements

This work was sponsored by National Key R & D Program of China (Grant number: 2023YFC3009400), and Post-Doctoral Research Project of Jiangxi Province (Grant number: 2021KY59). The authors appreciate their supports.

Appendix A:. The time-history curves of interface shear displacement for the specimens under stepwise loading with varying moisture contents of the soil

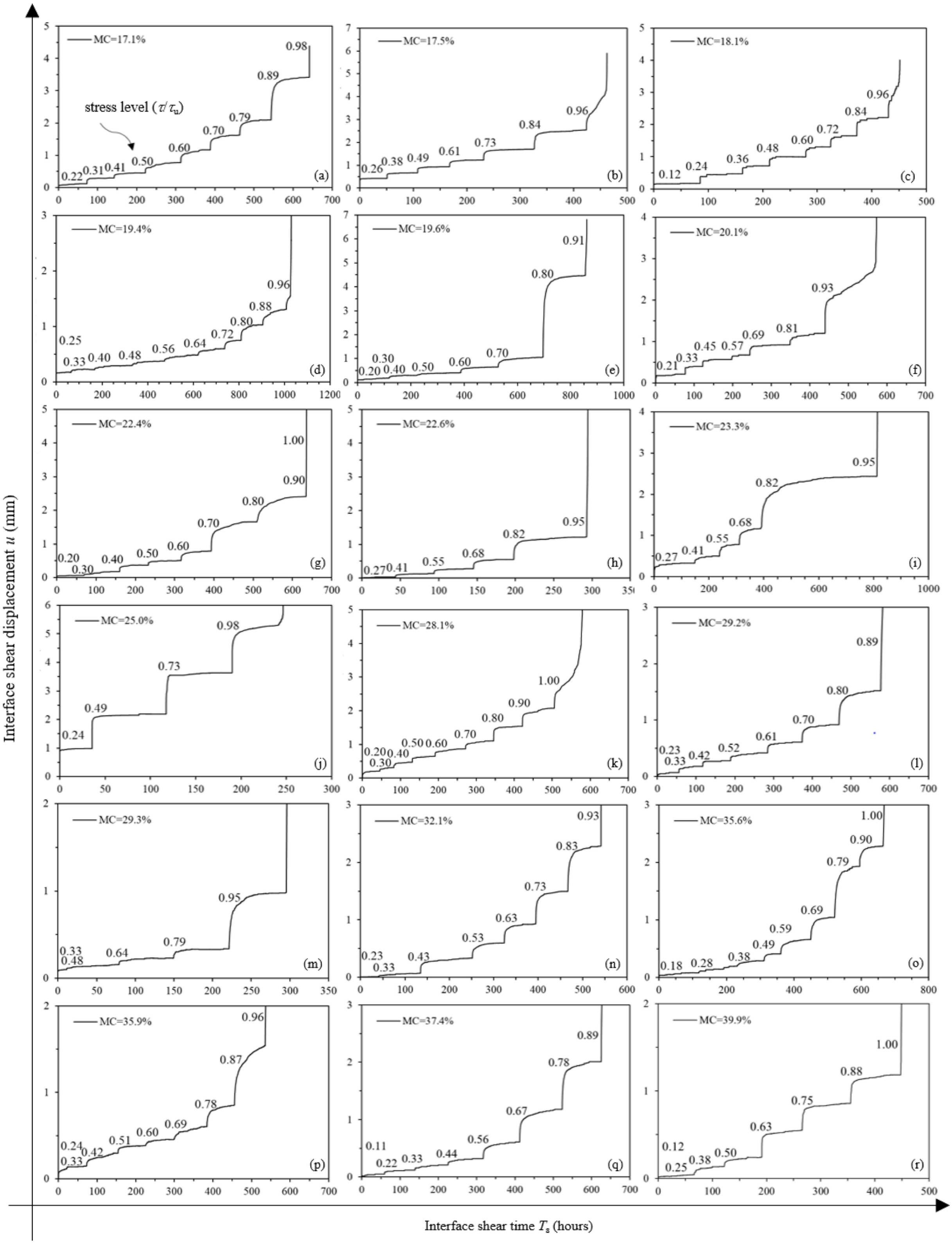

Appendix B:. The creep curves of interface shear displacement for the specimens under each single loading step with varying moisture contents of the soil

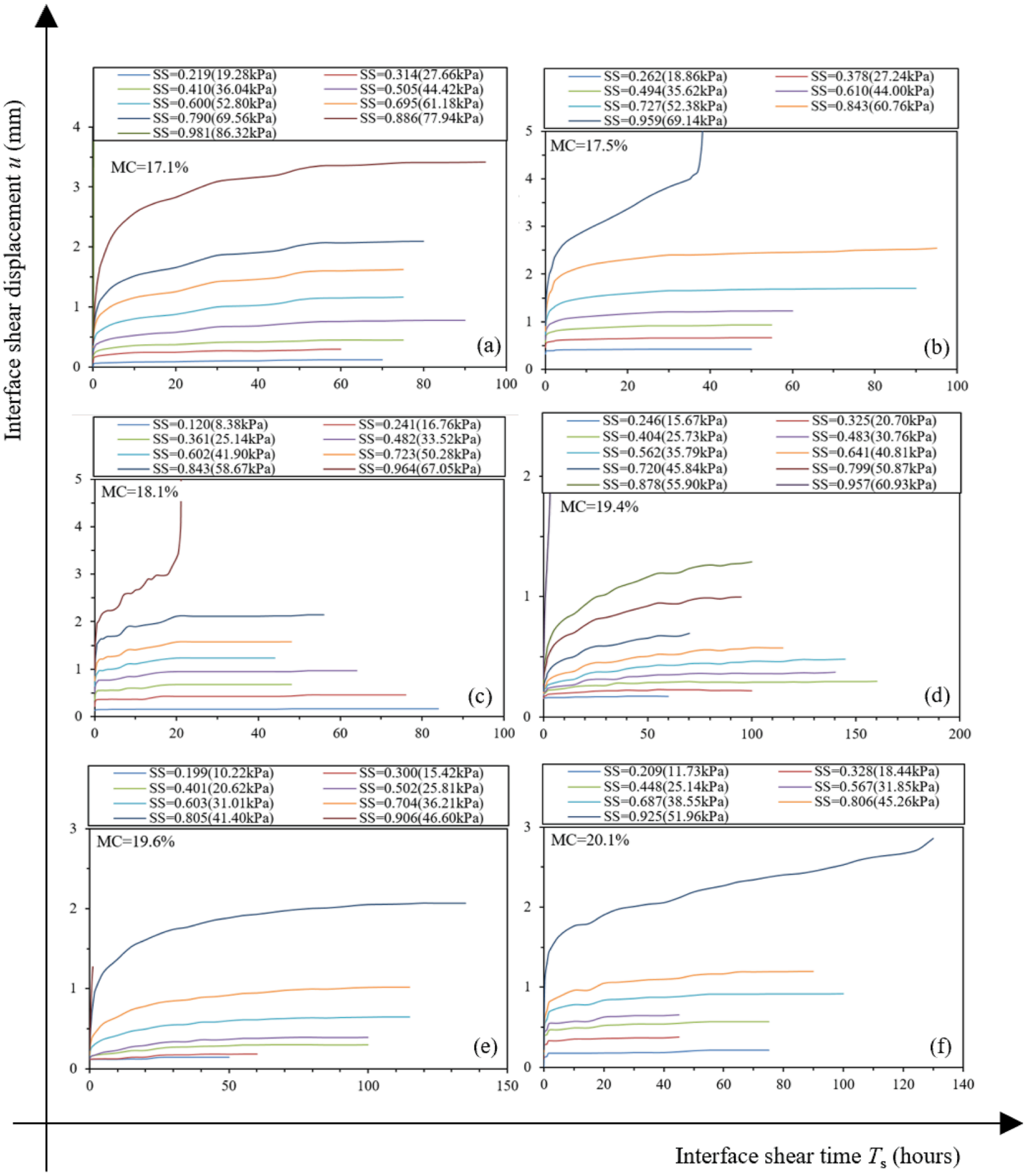

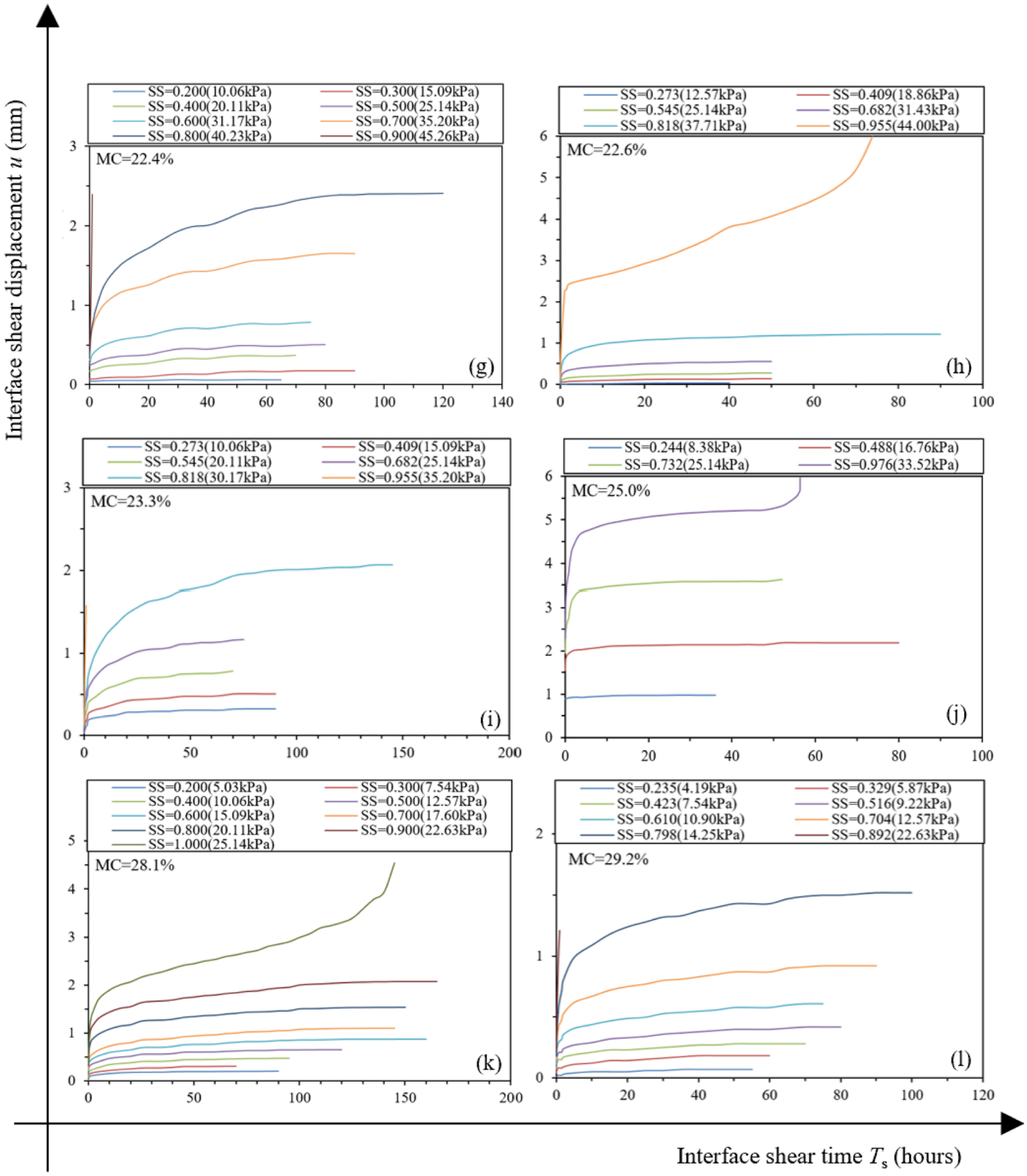
Interface shear displacement u (mm)
Interface shear time T_s (hours)
SS=0.200(10.06kPa)
SS=0.300(15.09kPa)
SS=0.400(20.11kPa)
SS=0.500(25.14kPa)
SS=0.600(31.17kPa)
SS=0.700(35.20kPa)
SS=0.800(40.23kPa)
SS=0.900(45.26kPa)
MC=22.4%
(g)
SS=0.273(12.57kPa)
SS=0.409(18.86kPa)
SS=0.545(25.14kPa)
SS=0.682(31.43kPa)
SS=0.818(37.71kPa)
SS=0.955(44.00kPa)
MC=22.6%
(h)
SS=0.273(10.06kPa)
SS=0.409(15.09kPa)
SS=0.545(20.11kPa)
SS=0.682(25.14kPa)
SS=0.818(30.17kPa)
SS=0.955(35.20kPa)
MC=23.3%
(i)
SS=0.244(8.38kPa)
SS=0.488(16.76kPa)
SS=0.732(25.14kPa)
SS=0.976(33.52kPa)
MC=25.0%
(j)
SS=0.200(5.03kPa)
SS=0.300(7.54kPa)
SS=0.400(10.06kPa)
SS=0.500(12.57kPa)
SS=0.600(15.09kPa)
SS=0.700(17.60kPa)
SS=0.800(20.11kPa)
SS=0.900(22.63kPa)
SS=1.000(25.14kPa)
MC=28.1%
(k)
SS=0.235(4.19kPa)
SS=0.329(5.87kPa)
SS=0.423(7.54kPa)
SS=0.516(9.22kPa)
SS=0.610(10.90kPa)
SS=0.704(12.57kPa)
SS=0.798(14.25kPa)
SS=0.892(22.63kPa)
MC=29.2%
(l)

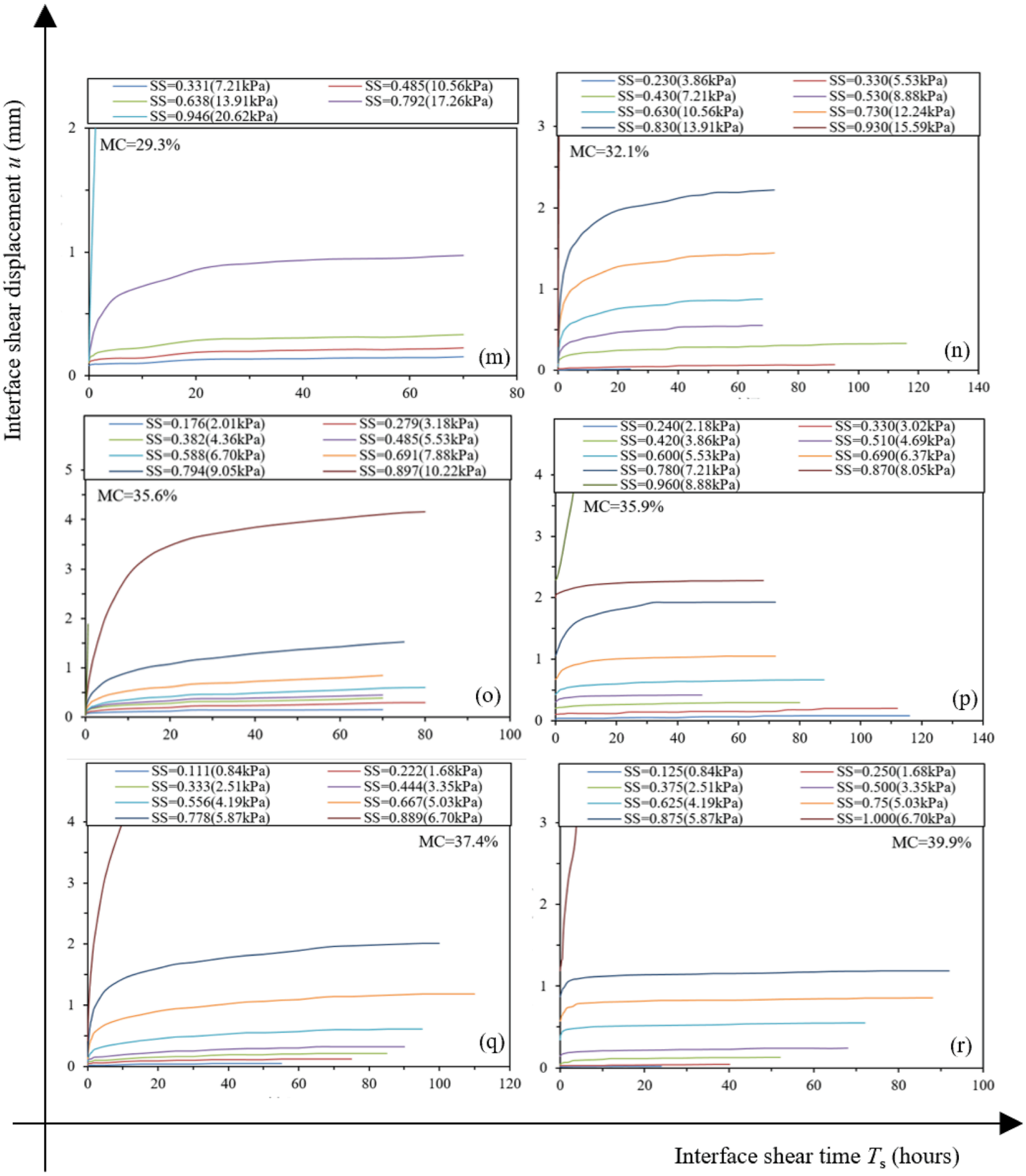
Interface shear displacement u (mm)
Interface shear time T_s (hours)
SS=0.331(7.21kPa)
SS=0.485(10.56kPa)
SS=0.638(13.91kPa)
SS=0.792(17.26kPa)
SS=0.946(20.62kPa)
MC=29.3%
(m)
SS=0.230(3.86kPa)
SS=0.330(5.53kPa)
SS=0.430(7.21kPa)
SS=0.530(8.88kPa)
SS=0.630(10.56kPa)
SS=0.730(12.24kPa)
SS=0.830(13.91kPa)
SS=0.930(15.59kPa)
MC=32.1%
(n)
SS=0.176(2.01kPa)
SS=0.279(3.18kPa)
SS=0.382(4.36kPa)
SS=0.485(5.53kPa)
SS=0.588(6.70kPa)
SS=0.691(7.88kPa)
SS=0.794(9.05kPa)
SS=0.897(10.22kPa)
MC=35.6%
(o)
SS=0.240(2.18kPa)
SS=0.330(3.02kPa)
SS=0.420(3.86kPa)
SS=0.510(4.69kPa)
SS=0.600(5.53kPa)
SS=0.690(6.37kPa)
SS=0.780(7.21kPa)
SS=0.870(8.05kPa)
SS=0.960(8.88kPa)
MC=35.9%
(p)
SS=0.111(0.84kPa)
SS=0.222(1.68kPa)
SS=0.333(2.51kPa)
SS=0.444(3.35kPa)
SS=0.556(4.19kPa)
SS=0.667(5.03kPa)
SS=0.778(5.87kPa)
SS=0.889(6.70kPa)
MC=37.4%
(q)
SS=0.125(0.84kPa)
SS=0.250(1.68kPa)
SS=0.375(2.51kPa)
SS=0.500(3.35kPa)
SS=0.625(4.19kPa)
SS=0.75(5.03kPa)
SS=0.875(5.87kPa)
SS=1.000(6.70kPa)
MC=39.9%
(r)

Appendix C:. The isochrone curves (interface shear stress-displacement curves at each specific time) for the specimens with varying moisture contents of the soil

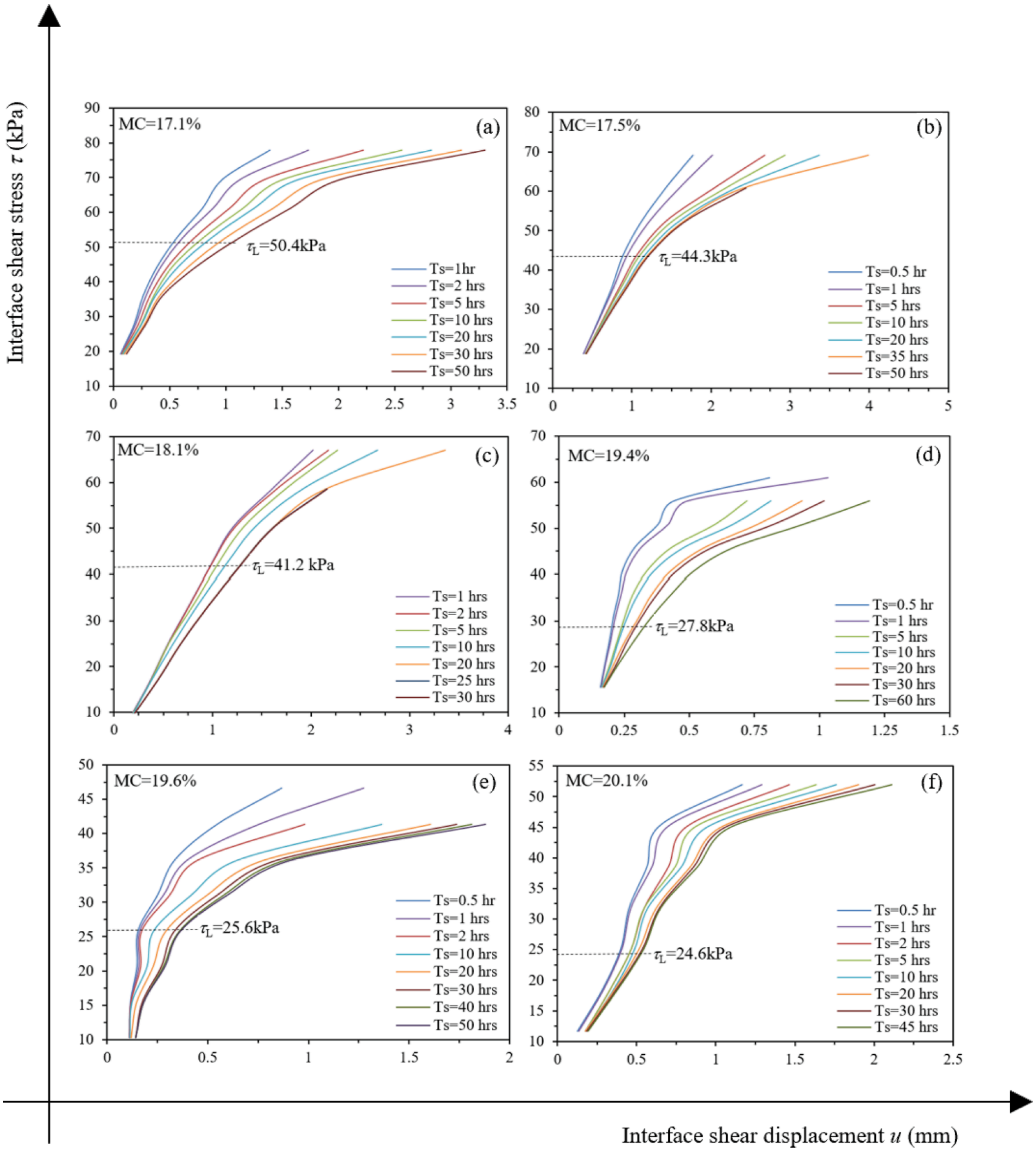

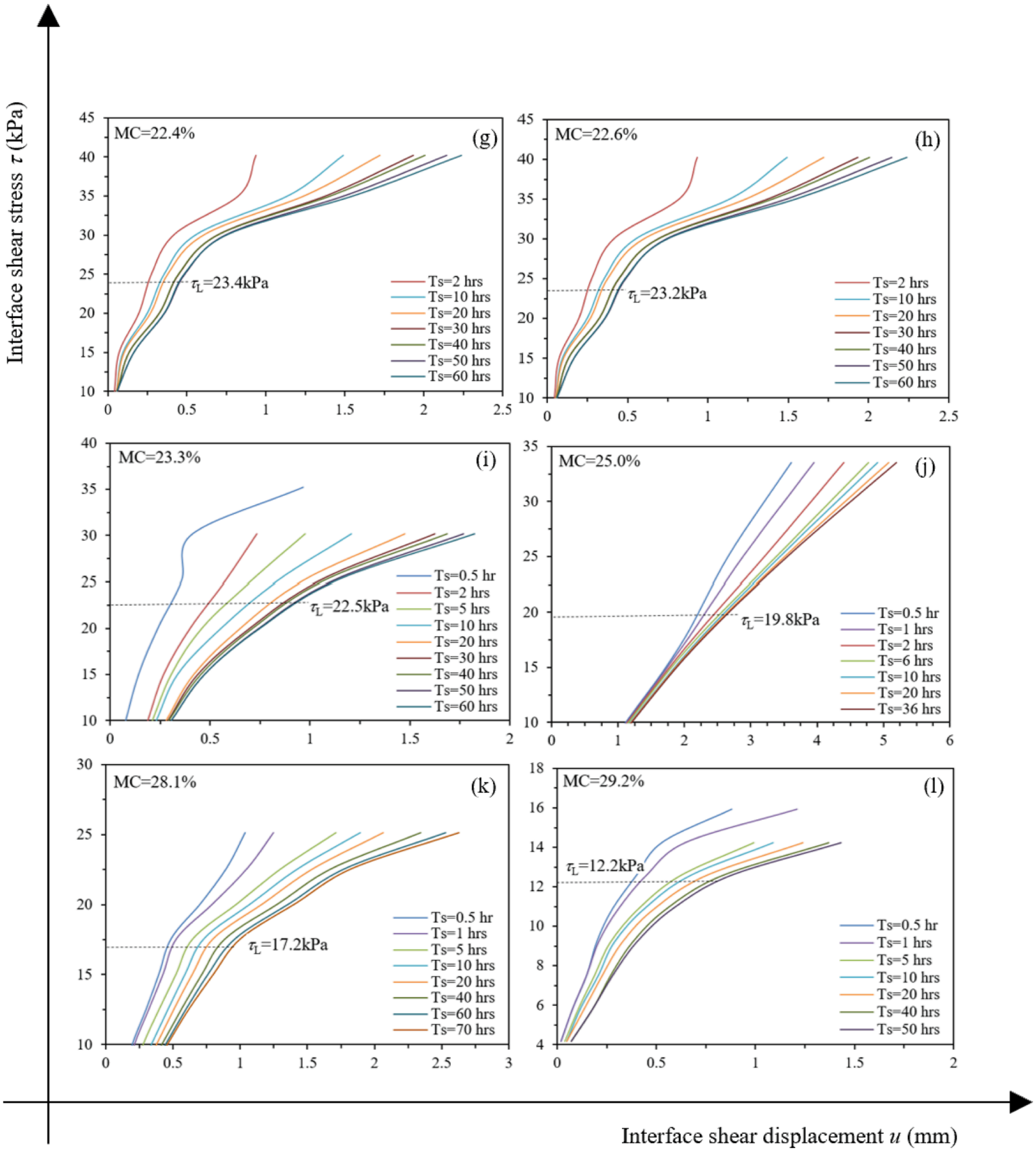
Interface shear stress τ (kPa)
Interface shear displacement u (mm)
MC=22.4%
(g)
τ_L=23.4kPa
Ts=2 hrs
Ts=10 hrs
Ts=20 hrs
Ts=30 hrs
Ts=40 hrs
Ts=50 hrs
Ts=60 hrs
MC=22.6%
(h)
τ_L=23.2kPa
Ts=2 hrs
Ts=10 hrs
Ts=20 hrs
Ts=30 hrs
Ts=40 hrs
Ts=50 hrs
Ts=60 hrs
MC=23.3%
(i)
τ_L=22.5kPa
Ts=0.5 hr
Ts=2 hrs
Ts=5 hrs
Ts=10 hrs
Ts=20 hrs
Ts=30 hrs
Ts=40 hrs
Ts=50 hrs
Ts=60 hrs
MC=25.0%
(j)
τ_L=19.8kPa
Ts=0.5 hr
Ts=1 hrs
Ts=2 hrs
Ts=6 hrs
Ts=10 hrs
Ts=20 hrs
Ts=36 hrs
MC=28.1%
(k)
τ_L=17.2kPa
Ts=0.5 hr
Ts=1 hrs
Ts=5 hrs
Ts=10 hrs
Ts=20 hrs
Ts=40 hrs
Ts=60 hrs
Ts=70 hrs
MC=29.2%
(l)
τ_L=12.2kPa
Ts=0.5 hr
Ts=1 hrs
Ts=5 hrs
Ts=10 hrs
Ts=20 hrs
Ts=40 hrs
Ts=50 hrs

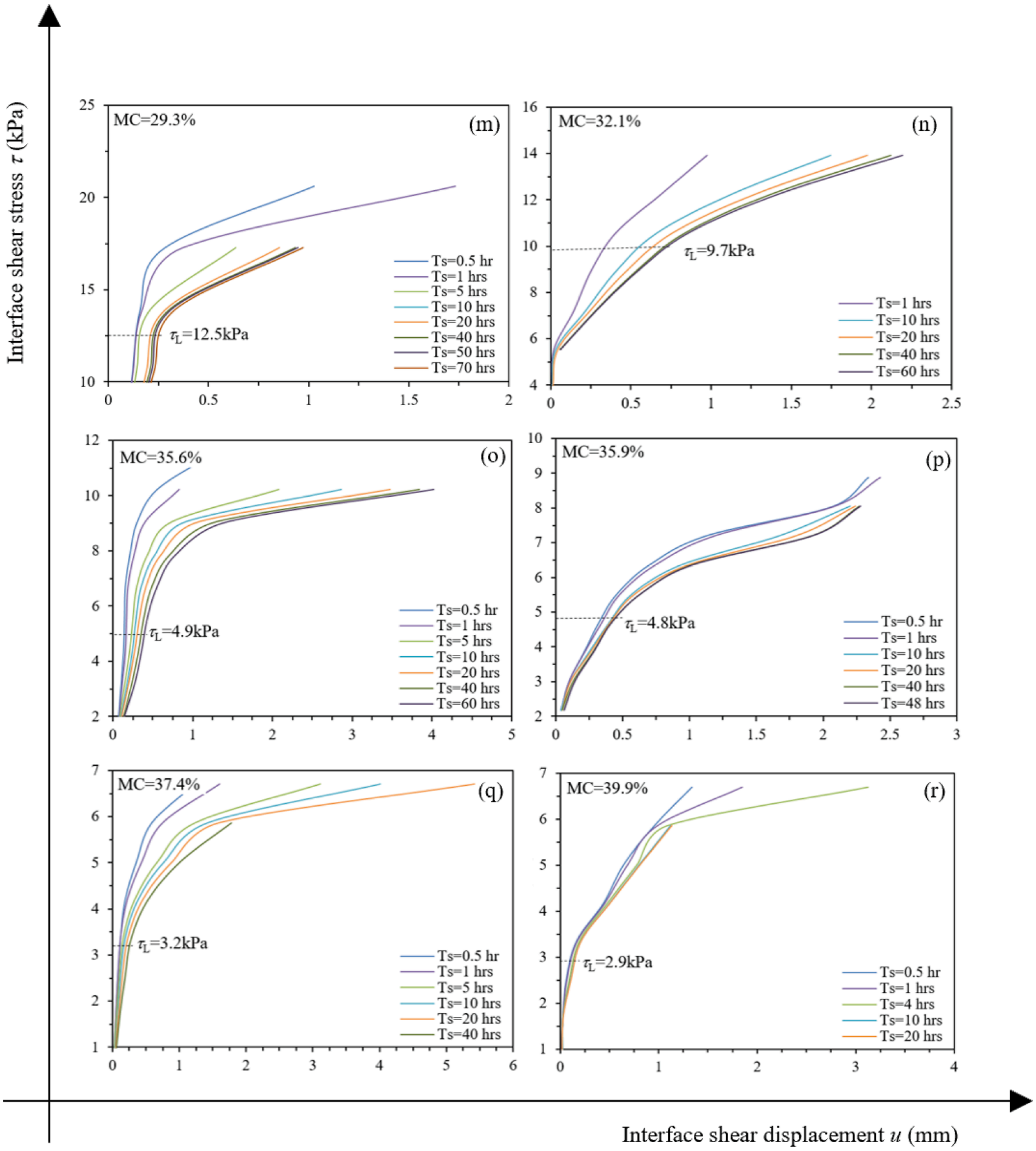

References

[1] Zinan Ara Urmi, Saeidi Ali, Yerro Alba, Chavali Rama Vara Prasad. Prediction of post-peak stress-strain behavior for sensitive clays. Eng Geol 2023;323. https://doi.org/10.1016/j.enggeo.2023.107221.

[2] Ran Chen, Bai Xiaoyong, Tan Qiu, Luo Guangjie, Cao Yue, Luhua Wu, Chen Fei, Li Chaojun, Luo Xuling, Liu Min. Threat of soil formation rate to health of karst ecosystem. Sci Total Environ 2023;887. https://doi.org/10.1016/j.scitotenv.2023.163911.

[3] Liu Chao, Cui Jie, Zhang Zixin, Liu Hai, Huang Xin, Zhang Changqiang. The role of TBM asymmetric tail-grouting on surface settlement in coarse-grained soils of urban area: Field tests and FEA modelling. Tunn Undergr Space Technol 2021;111. https://doi.org/10.1016/j.tust.2021.103857.

[4] Ehrlich Maurício, Silva Rafael Cerqueira. Behavior of a 31 m high excavation supported by anchoring and nailing in residual soil of gneiss. Eng Geol 2015;191: 48–60. https://doi.org/10.1016/j.enggeo.2015.01.028.

[5] Xu Xi, Huang Yu, Yashima Atsushi, Du Xiuli. Failure evolution process of pile-anchor reinforced rock slope based on centrifuge shaking table tests. Eng Geol 2022;311. https://doi.org/10.1016/j.enggeo.2022.106920.

[6] Zhou Chang, Ma Wenchao, Sui Wanghua. Transparent soil model test of a landslide with umbrella-shaped anchors and different slope angles in response to rapid drawdown. Eng Geol 2022;307. https://doi.org/10.1016/j.enggeo.2022.106765.

[7] Zhipeng Wu, Jian Xu, Li Yanfeng, Wang Songhe. Disturbed state concept–based model for the uniaxial strain-softening behavior of fiber-reinforced soil. Int J Geomech 2022;22(7). https://doi.org/10.1061/(ASCE)GM.1943-5622.0002415.

[8] Benmokrane Brahim, Ballivy Gerard. Five-year monitoring of load losses on prestressed cement-grouted rock anchors. Can Geotech J 1991;28(5):668–77. https://doi.org/10.1139/t91-081.

[9] Benmokrane B, Chennouf A, Mitri HS. Laboratory evaluation of cement-based grouts and grouted rock anchors. In: International journal of rock mechanics and mining sciences & geomechanics abstracts. 1995. Elsevier.

[10] Sebastian Bryson L, Giraldo Jorge Romana. Analysis of case study presenting ground anchor load-transfer response in shale stratum. Can Geotech J 2020;57(1): 85–99. https://doi.org/10.1139/cgj-2018-0326.

[11] Li-Jun Su, Chan Terence CF, Shiu YK, Cheung Tony, Yin Jian-Hua. Influence of degree of saturation on soil nail pull-out resistance in compacted completely decomposed granite fill. Can Geotech J 2007;44(11):1314–28. https://doi.org/10.1139/T07-056.

[12] Zhang Genbao, Chen Changfu, Zornberg Jorge G, Morsy Amr M, Mao Fengshan. Interface creep behavior of grouted anchors in clayey soils: effect of soil moisture condition. Acta Geotech 2020;15:2159–77. https://doi.org/10.1007/s11440-019-00907-6.

[13] Chen Changfu, Zhu Shimin, Zhang Genbao, Morsy Amr M, Zornberg Jorge G, Mao Fengshan. A generalized load-transfer modeling framework for tensioned anchors integrating adhesion–friction-based interface model. Int J Geomech 2022; 22(5). https://doi.org/10.1061/(ASCE)GM.1943-5622.0002338.

[14] Chen Changfu, Zhu Shimin, Zhang Genbao, Mao Fengshan, Cai Huan. Time-dependent load transfer behavior of grouted anchors in laterite. Comput Geotech 2021;132. https://doi.org/10.1016/j.compgeo.2020.103969.

[15] Zhu Shimin, Chen Changfu, Zhang Genbao, Cheng Du. Theoretical and experimental investigations of anchoring force loss behavior for prestressed ground anchors. Can Geotech J 2022;59(9):1587–601. https://doi.org/10.1139/cgj-2021-0220.

[16] Chen Changfu, Zhu Shimin, Zhang Genbao, Morsy Amr M, Zornberg Jorge G, Huang Jiabin. Interface creep behavior of tensioned GFRP tendons embedded in cemented soils. Geosynth Int 2022;29(3):241–53. https://doi.org/10.1680/jgein.21.00008.

[17] Zhu Shimin, Chen Changfu, Cheng Du. Interface stress relaxation behavior of grouted anchors in red clay: experimental study and a disturbed state concept-based theoretical model. Acta Geotech 2023;18(6):3287–306. https://doi.org/10.1007/s11440-022-01693-4.

[18] Changfu Chen, Shimin Zhu, Fengshan Mao, Genbao Zhang. Characterization and modelling of coupled consolidation-creep behavior of red clay. 工程地质学报 2019;27(4):723–8. https://doi.org/10.13544/j.cnki.jeg.2018-330.

[19] Yuan Jie, Wang Tao Jin, Chen Jian, Huang Jian An. Microscopic mechanism study of the creep properties of soil based on the energy scale method. Front Mater 2023;10. https://doi.org/10.3389/fmats.2023.1137728.

[20] Li Jianbo, Chen Miaomiao, Li Zhiyuan. Improved soil–structure interaction model considering time-lag effect. Comput Geotech 2022;148. https://doi.org/10.1016/j.compgeo.2022.104835.

[21] Hossain Md Akhtar, Jian-Hua Yin. Influence of grouting pressure on the behavior of an unsaturated soil-cement interface. J Geotech Geoenviron Eng 2012;138(2):193–202. https://doi.org/10.1061/(ASCE)GT.1943-5606.0000585.

[22] Chang-Fu Chen, Guan-Ting Liang, Tang Yu, You-Lin Xu. Anchoring solid-soil interface behavior using a novel laboratory testing technique. Chinese. J Geotech Eng 2015;37(6):1115–22. https://doi.org/10.11779/CJGE201506018.

[23] Chen Changfu, Zhang Genbao, Zornberg Jorge Gabriel, Zheng Xinxiu. Element nail pullout tests for prediction of soil nail pullout resistance in expansive clays. Geotech Test J 2019;42(5):1274–97. https://doi.org/10.1520/GTJ20170431.

[24] Mahmoodzadeh Arsalan, Mohammadi Mokhtar, Ibrahim Hawkar Hashim, Abdulhamid Sazan Nariman, Salim Sirwan Ghafoor, Hunar Farid Hama Ali. Artificial intelligence forecasting models of uniaxial compressive strength. Transp Geotech 2021;27. https://doi.org/10.1016/j.trgeo.2020.100499.

[25] Zhang Genbao, Chen Changfu, Sun Junbo, Li kefei, Xiao Fan, Wang Yufei, et al. *Mixture optimisation for cement-soil mixtures with embedded GFRP tendons.* J Mater Res Technol 2022. **18**: p. 611-628 DOI: 10.1016/j.jmrt.2022.02.076.

[26] Zhang Genbao, Chen Changfu, Zhang Yuhao, Zhao Hongchao, Wang Yufei, Wang Xiangyu. Optimised neural network prediction of interface bond strength for GFRP tendon reinforced cemented soil. Geomech Eng 2022;28(6):599–611. https://doi.org/10.12989/gae.2022.28.6.599.

[27] Won Jongmuk, Tutumluer Erol, Byun Yong-Hoon. Predicting permanent strain accumulation of unbound aggregates using machine learning algorithms. Transp Geotech 2023;42. https://doi.org/10.1016/j.trgeo.2023.101060.

[28] Duan Shuqian, Zhang Minghuan, Dingping Xu, Xiong Jiecheng, Yujun Cui YuSu. Mechanical response and data-driven fatigue model of interlayer soils in track-bed considering multi-factor coupling effect. Comput Geotech 2023;163. https://doi.org/10.1016/j.compgeo.2023.105749.

[29] Duan Shuqian, Zhao Gengchen, Jiang Quan, Xiong Jiecheng, Sun Yuanda, Kou Yongyuan, et al. Multi-index fusion database and intelligent evaluation modelling for geostress classification. Tunn Undergr Space Technol 2024;149. https://doi.org/10.1016/j.tust.2024.105802.

[30] Pham Khanh, Le Dongku Kim V, Canh Jongmuk Won. Machine learning-based pedotransfer functions to predict soil water characteristics curves. Transp Geotech 2023;42. https://doi.org/10.1016/j.trgeo.2023.101052.

[31] Lin Peiyuan, Chen Xianying, Jiang Mingjie, Song Xugen, Meijuan Xu, Huang Sheng. Mapping shear strength and compressibility of soft soils with artificial neural networks. Eng Geol 2022;300. https://doi.org/10.1016/j.enggeo.2022.106585.

[32] Tjong-Kie Tan, Wen-Fa Kang. Locked in stresses, creep and dilatancy of rocks, and constitutive equations. Rock Mech 1980;13:5–22. https://doi.org/10.1007/BF01257895.

[33] Liu Lin, Weiya Xu. Experimental researches on long-term strength of granite gneiss. p. 2: 1–9 Adv Mater Sci Eng 2015. https://doi.org/10.1155/2015/187616.

[34] Tan Tjong Kie. The mechanical problems for the long-term stability of underground galleries. Chin J Rock Mech Eng 1982;1(1):1–20.

[35] Sun Junbo, Wang Yufei, Yao Xupei, Ren Zhenhua, Zhang Genbao, Zhang Chao, et al. Machine-learning-aided prediction of flexural strength and ASR expansion for waste glass cementitious composite. Appl Sci 2021;11(15):6686.

[36] Ni Tianming, Liu Dongsheng, Qi Xu, Huang Zhengfeng, Liang Huaguo, Yan Aibin. Architecture of cobweb-based redundant TSV for clustered faults. IEEE Trans Very Large Scale Integr VLSI Syst 2020;28(7):1736–9. https://doi.org/10.1109/TVLSI.2020.2995094.

[37] Feng Wanhui, Wang Yufei, Sun Junbo, Tang Yunchao, Dongxiao Wu, Jiang Zhiwei, et al. Prediction of thermo-mechanical properties of rubber-modified recycled aggregate concrete. Constr Build Mater 2022;318.

[38] Liu Yang, Zhao Qingzhi, Yao Wanqiang, Ma Xiongwei, Yao Yibin, Liu Lilong. Short-term rainfall forecast model based on the improved BP–NN algorithm. Sci Rep 2019;9(1):1–12.

[39] Zhang Tao, Wang Cai-Jin, Liu Song-Yu, Zhang Nan, Zhang Tong-Wei. Assessment of soil thermal conduction using artificial neural network models. Cold Reg Sci Technol 2020;169.

[40] Erdal Hamit, Karahanoğlu Ilhami. Bagging ensemble models for bank profitability: An emprical research on Turkish development and investment banks. Appl Soft Comput 2016;49:861–7.

[41] Sun Junbo, Ma Yongzhi, Li Jianxin, Zhang Junfei, Ren Zhenhua, Wang Xiangyu. Machine learning-aided design and prediction of cementitious composites containing graphite and slag powder. J Build Eng 2021.

[42] Breiman Leo. Bagging predictors. Mach Learn 1996;24(2):123–40. https://doi.org/10.1007/BF00058655.

[43] Whigham Peter A, Owen Caitlin A, Macdonell Stephen G. A baseline model for software effort estimation. ACM Trans Software Eng Methodol (TOSEM) 2015;24(3):1–11.

[44] Sun Junbo, Zhang Junfei, Yunfan Gu, Huang Yimiao, Sun Yuantian, Ma Guowei. Prediction of permeability and unconfined compressive strength of pervious concrete using evolved support vector regression. Constr Build Mater 2019;207:440–9. https://doi.org/10.1016/j.conbuildmat.2019.02.117.

[45] Sun Yuantian, Zhang Junfei, Li Guichen, Wang Yuhang, Sun Junbo, Jiang Chao. Optimized neural network using beetle antennae search for predicting the unconfined compressive strength of jet grouting coalcretes. Int J Numer Anal Meth Geomech 2019;43(4):801–13.

[46] Cunningham Padraig, Delany Sarah Jane. k-Nearest neighbour classifiers-A Tutorial. ACM computing surveys (CSUR) 2021;54(6):1–25.

[47] Wang Jiangyu, Chen Huanxin. *BSAS: Beetle swarm antennae search algorithm for optimization problems.* arXiv preprint arXiv:1807.10470, 2018.

[48] Tang Yunchao, Wang Yufei, Dongxiao Wu, Liu Zhonghe, Zhang Hexin, Zhu Ming, et al. An experimental investigation and machine learning-based prediction for seismic performance of steel tubular column filled with recycled aggregate concrete. Rev Adv Mater Sci 2022;61(1):849–72.

[49] Sun Junbo, Wang Jiaqing, Zhu Zhaoyue, He Rui, Peng Cheng, Zhang Chao. Mechanical performance prediction for sustainable high-strength concrete using bio-inspired neural network. Buildings 2022;12(1):65.

[50] Zhang Junfei, Huang Yimiao, Ma Guowei, Nener Brett. Mixture optimization for environmental, economical and mechanical objectives in silica fume concrete: A novel frame-work based on machine learning and a new meta-heuristic algorithm. Resour Conserv Recycl 2021;167.

[51] Zhang Genbao, Ding Zhiqing, Wang Yufei, Guihai Fu, Wang Yan, Xie Chenfeng, et al. Performance prediction of cement stabilized soil incorporating solid waste and propylene fiber. Materials 2022;15(12):4250.

[52] Yao Xiaofei, Lyu Xin, Sun Junbo, Wang Bolin, Wang Yufei, Yang Min, et al. AI-based performance prediction for 3D-printed concrete considering anisotropy and steam curing condition. Constr Build Mater 2023;375.

[53] Friedman Jerome H. Greedy function approximation: a gradient boosting machine. Ann Stat 2001:1189–232.

[54] Wang Binghui, Gong Neil Zhenqiang. Stealing hyperparameters in machine learning. In: 2018 IEEE symposium on security and privacy (SP). 2018. IEEE.